CONFERENCE PROCEEDINGS

7th INTERNATIONAL CONFERENCE ON BIOTECHNOLOGY FOR THE THE WELLNESS INDUSTRY

"Bioresources for Human Wellness"

ORGANIZED BY

UTM Universiti Teknologi Malaysia | Institute of Bioproduct Development

CO-ORGANIZERS

Innovation Centre in Agritechnology for Advanced Bioprocessing, UTM

Faculty of Engineering, UTM

Kementerian Pendidikan Malaysia

National University Corporation Shizuoka University

أكاديمية البحث العلمي والتكنولوجيا
Academy of Scientific Research & Technology

جامعة أبوظبي
ABU DHABI UNIVERSITY

dongguk UNIVERSITY

CCERCI

RUDN university

TALLINN UNIVERSITY OF TECHNOLOGY

Curtin University Malaysia

eISBN 978-983-99322-5-6

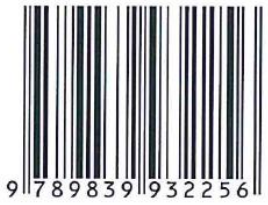

Printed in Malaysia by:

Institute of Bioproduct Development,
Universiti Teknologi Malaysia
www.ibd.utm.my

http://www.utm.my/ibd/icbwi2018/

7th INTERNATIONAL CONFERENCE ON BIOTECHNOLOGY FOR THE WELLNESS INDUSTRY

(7th ICBWI 2018)

27th – 28th November 2018
Universiti Teknologi Malaysia
Kuala Lumpur

Editors

Norhayati Mohamed Noor
A Rafidah A Mohd Yunos
Ida Madiha Yusoff

TABLE OF CONTENT

TRACK 4: AGRI-BIOTECHNOLOGY

TRACK 5: PRODUCT FORMULATION AND CONTROLLED RELEASE FOR WELLNESS INDUSTRIES

TRACK 7: PLANT AND HERBAL BIOPROCESSING STANDARDIZATION AND PROFILING

TRACK 8: TISSUE ENGINEERING

TRACK 9: OMIC TECHNOLOGIES

KINETIC ANALYSIS OF BIOHYDROGEN FORMATION FROM PINEAPPLE RESIDUES USING IMMOBILIZED BACATERIA CO-CULTURE ON ACTIVATED CARBON SPONGE

Nur Kamilah Abd Jalil[1], Aishah Abd Jalil[1,2], Arshad Ahmad[1,2], Umi Aisah Asli*[2,3], Aidee Kamal Khamis[2,3], Haslenda Hashim, Ho Wai Shin[1,4],

[1]*Faculty of Chemical and Energy Engineering, U, 81310 Johor Bahru, Johor, Malaysia*

[2]*Centre of Hydrogen Energy, Institute of Future Energy, Universiti Teknologi Malaysia, 81310 Johor Bahru, Johor, Malaysia*

[3]*Innovation Centre in Agritechnology for Advanced Bioprocessing (ICA), UTM Pagoh Research Center, 86400 Pagoh, Malaysia*

[4]*Process Systems Engineering Centre, Universiti Teknologi Malaysia, 81310 Johor Bahru, Johor, Malaysia*

ABSTRACT

In this work, a kinetic analysis for fermentative biohydrogen production using different hydrogen-producing bacteria onto activated carbon sponge has been done. The fermentation experiment was carried out using pineapple residues with 30 % inoculum of working volume at the temperature of 32 °C and pH condition of 7. Three different H_2-producing bacteria were used namely *Escherichia coli*, *Enterobacter. aerogenes* and *Clostridium sporogenes*, which immobilized onto carbon sponge and also in free cell form as comparison. The modified Gompertz equation was used for the kinetic of cumulative biohydrogen production via Excel solver application. Based on best fitting curve result for the cumulative biohydrogen production, it was found that modified Gompertz equation were fitted well with all the experimental results of all regression values, R^2 were greater than 0.9. The modified Gompertz equation would be useful for other analysis of biohydrogen production performance using selected H_2-producing bacteria culture onto activated carbon sponge from pineapple residues.

Keywords: Kinetic analysis; Gompertz model; bacteria co-culture; immobilization; biohydrogen; pineapple residues

1. INTRODUCTION

Kinetic modelling is very important in production of biohydrogen as growth associated product (Singh *et al*., 2015). Different model has been tested in order to improve or analyse the effect, relationship, and role of the parameter and predict the performance of biohydrogen during fermentation. Table 1 displays the model and function in biohydrogen production (Singh *et al*., 2015);

The modified Gompertz equation has been widely used for the performance of biohydrogen production by fermentation which defined as follow:

$$P_t = \mathrm{P}_m \left\{ - \exp\left[\frac{R_m \times e}{P_m} (\lambda - t) + 1 \right] \right\}$$

Where P_t is the cumulative biohydrogen production (mL) at culture time t, P_m is the maximum amount of biohydrogen production (mL/L), R_m is the maximum biohydrogen production rate (mL/L/hr), λ is the lag time (h) and the value of e is 2.71828. The correlation coefficient (R^2 value range over 0.99) indicating a strong correlation between the experimental data and the fit (modified Gompertz equation) definitely describe the formation of biohydrogen.

Table 1. Kinetic Modelling of Biohydrogen Production

No	Models	Functions
1	Arrhenius	Effect of temperature on H_2 production
2	Monod or Michaelis-Menten	Microbial growth on H_2 production
3	Logistic	Describe bacterial cell growth
4	Haldane-Andrew and Hans-Levenspiel	Substrate inhibition or substrate dependent on specific growth
5	Leudeking-Piret	Relation between cell growth and H_2 production rate
6	Andrew	Relation between pH and substrate consumption
7	Gompertz	Progress of cumulative H_2 production

Besides the biohydrogen production, this equation also works to describe the progress of bacteria growth and substrate degradation (Boni et al., 2013). Other than that, other equations also been used by researchers to investigate the effect of different parameters that influence fermentative hydrogen production. It is based on the kinetic constant obtained from the models.

2. METHODOLOGY

2.1 Pre-Treatment of Pineapple Substrate

Pineapple waste was obtained from local market in Johor Bahru. The pineapple peel was selected to be processed as hydrolysate or substrate to be used in the fermentation. The substrate undergo steam heat pre-treatment (autoclaved) before being chopped into small pieces. Afterwards, the chopped pineapple waste was crushed using the steel blender (Waring Commercial Blender) with distilled water in ratio of 1: 2. Next, the mixture was filtrate to obtain the hydrolysate or extract for the characterization analysis. The hydrolysate then stored in refrigerator at 4 ˚C and restored to ambient temperature, 25 ℃ before used. The hydrolysate will be neutralized to pH 7 before mixed with inoculum and used as substrate for the fermentation.

2.2 Culture activation and Cultivation

Facultative anaerobes (*Enterobacter aerogenes* - ATCC 13048 and *Escherichia coli* – ATTC 10799) and so known strict anaerobes bacteria (*Clostridium sporogenes* – ATCC 19404) purchased from Microbiologics were utilized as co-culture to perform the fermentation process. For inoculum (co-culture) preparation, each co-culture of bacteria were activated on agar medium and cultivated individually in nutrient broth carefully and aseptically for 24 hours (overnight) in incubator.

2.3 AC Selection and Pre-treatment

Commercial activated carbon sponge was used as support materials for co-culture bacteria to retain. The AC sponge were cut into pieces (1 ± 0.2 cm x 1 ± 0.2 cm) and soaked in boiling water for 30 minutes. Then, the sponges were washed under tap water before left in distilled water for 24 h (changed 3-4 times). This is essential to remove all fine suspended particles (Rahma, 2013). Next, the sponges were dried in oven at 70 ˚C overnight before uniformly dried in desiccator.

2.4 Experimental Design

2.4.1 Immobilization of Co-culture on AC

There are three different H_2-producing bacteria types used in this work, *E. coli*, *E. aerogenes* and *C. sporogenes* which are labelled as A, B, and C accordingly. Each type was co-cultured each other, to make three combinations, i) A and B, ii) B and C and iii) A and C. The co-culture were mixed

together with the immersion of AC sponges inside 90 ml of respective co-culture (30% of working volume) to be incubated for another 24 hours at 130 r.p.m at 37 ˚C before used.

2.4.2 Immobilization of Co-culture on AC

There are three different H_2-producing bacteria types used in this work, *E. coli*, *E. aerogenes* and *C. sporogenes* which are labelled as A, B, and C accordingly. Each type was co-cultured each other, to make three combinations, i) A and B, ii) B and C and iii) A and C. The co-culture were mixed together with the immersion of AC sponges inside 90 ml of respective co-culture (30% of working volume) to be incubated for another 24 hours at 130 r.p.m at 37 ˚C before used.

2.4.3 Fermentation of Immobilized Co-Culture On AC Sponges

The batch fermentation of pineapple substrate was carried out in 500 mL Dreschel bottle with the working volume of 300 ml. The 210 ml pineapple waste was first added to a 500 mL dreschel bottle and another 90 ml was the inoculum with immobilized co-culture on AC sponges. The initial pH of the substrate was adjusted using 0.5 M sodium hydroxide (NaOH) to achieve initial pH of 7. Nitrogen sparging was applied to provide anaerobic condition for the fermentation process and the bottles were sealed and put in a water bath to keep the culture medium at temperature 33 ℃ ±1 ℃. Mixing was provided by a stirring magnetic bar in the bottle.

3. RESULTS AND DISCUSSION

3.1 Kinetic Analysis with of free cell A,B,C, A/B, B/C and A/C

The result of cumulative biohydrogen production is shown in Figure 1. The values were used to fit the modified Gompertz equation as following where the maximum potential hydrogen formation (P_m), the maximum rate of hydrogen formation in ml/hr (R_m) and the lag phase (λ) of each culture and co-cultures type for free cell are shown in Table 2.

Results of fitting curve on Figure 1 and Table 2 illustrated that biohydrogen production fitted well with the modified Gompertz equation.

Table 2. Fermentation Results of free cells

Group	H_2 production (mL)	P (mL)	R_m (mL/L)	λ (h)	R_2
A	61.06	72.34	1.38	0.60	0.939
B	117.34	143.99	3.05	01.84	0.971
C	93.57	90.76	5.44	1.33	0.989
A/B	106.53	104.32	4.55	5.66	0.981
B/C	67.27	61.37	4.71	1.71	0.976
A/C	195.46	202.45	7.16	2.38	0.984

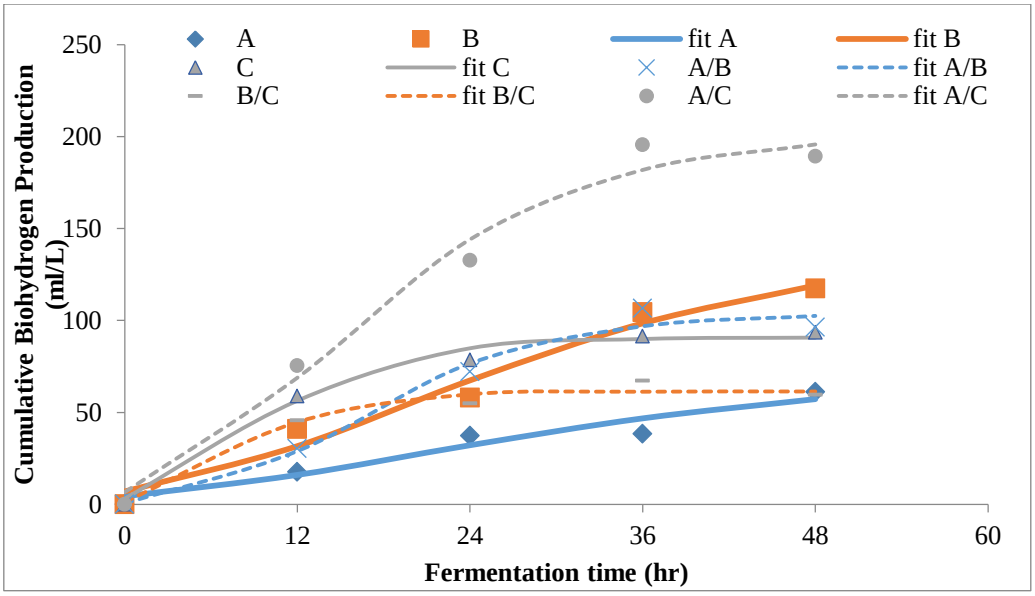

Figure 1. Cumulative biohydrogen production of free culture of A,B,C, A/B, B/C and A/C

The data presented were correlated with the Gompertz equation and the constants were determined by regression analysis based on biohydrogen cumulative curves. The curve fitting showed that the equation was suitable to describe the progress of cumulative biohydrogen production from pineapple substrate. These result showed that the optimum co-culture combination are A/C with corresponding biohydrogen production of 490.43 ml/L which is significantly higher compared to B/C and A/B production.

3.2 Kinetic Analysis of immobilized cell A, B, C, A/B, B/C and A/C on AC sponge

The result of cumulative biohydrogen production is shown in Figure 4.11. The values were used to fit the modified Gompertz equation as following where the maximum potential hydrogen formation (P_m), the maximum rate of hydrogen formation in ml/L/hr (R_m) and the lag phase, hr (λ) of each culture and co-cultures type for free cell are shown in Table 3.

Results of fitting curve on Figure 2 and Table 3 illustrated that biohydrogen production fitted well with the modified Gompertz equation.

Table 3. Fermentation result of immobilized co-cultures

Group	H_2 production (mL)	P (mL)	R_m (mL/L)	λ (h)	R_2
A	106.53	283.72	17.20	9.60	0.966
B	67.27	271.19	0.26	4	0.466
C	273.73	283.42	10.11	6.14	0.998
A/B	126.91	126.91	3.90	5.13	0.984
B/C	76.72	241.86	1.72	0	0.920
A/C	513.97	513.63	25.03	10.12	0.998

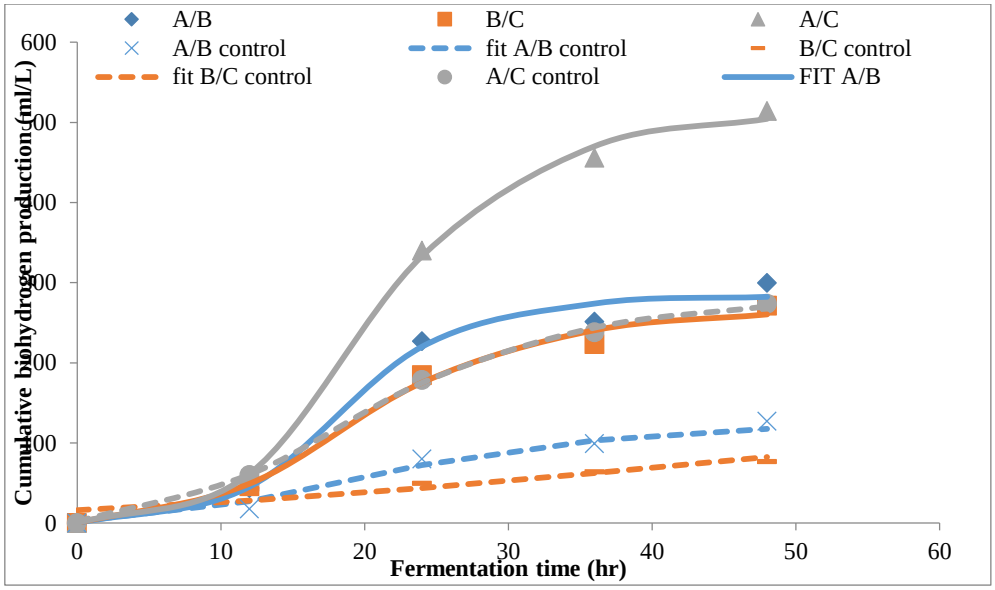

Figure 2. Cumulative biohydrogen production of immobilized co-culture of A,B,C, A/B, B/C and A/C

The combination of *E.coli* and *C. sporogenes* (A/C) as co-culture immobilized on AC sponge produced the highest rate of biohydrogen of 62.31 mmol/h/$L_{substrate}$ which 4.7 times compared than *E. aerogenes* and *C. sporogenes* (B/C) and 2.4 times with *E.coli* and *E.aerogenes* (A/B) after 24 hours presentation. The interactive effect of the co-culture and stable environment provided by AC sponge are the key for better production and performance of immobilized co-culture system.

4. CONCLUSION

This study has concluded that combination of *E.coli* and *C. sporogenes* (A/C) as co-culture immobilized on AC sponge produced the highest rate of biohydrogen of 62.31 mmol/h/$L_{substrate}$ which 4.7 times compared than *E. aerogenes* and *C. sporogenes* (B/C) and 2.4 times with *E.coli* and *E.aerogenes* (A/B) after 24 hours presentation. The interactive effect of the co-culture and stable environment provided by AC sponge are the key for better production and performance of immobilized co-culture system.

ACKNOWLEDGEMENT

The authors acknowledge the support by the Malaysian Ministry of Higher Education (MOHE) and GUP UTM research grant (Q.J10030000.2644.06J00, Q.J10030000.2644.09J17 and Q.J130000.2544.09H24) for funding the research.

REFERENCES

Boni, M. R., Sbaffoni, S., Tuccinardi, L., & Viotti, P. (2013). Development and calibration of a model for biohydrogen production from organic waste. *Waste Management (New York, N.Y.)*, *33*(5), 1128–35. https://doi.org/10.1016/j.wasman.2013.01.019

Rahma, A. A. (2013). Biohydrogen Production by Modified Anaerobic Fluidized Bed Reactor (AFBR) Using Mixed Bacterial Cultures in Thermophilic Condition . □†Š

Singh, A., Sevda, S., Reesh, I. M. A., & Vanbroekhoven, K. (2015). Biohydrogen Production from Lignocellulosic Biomass : Technology and Sustainability, 13062–13080. https://doi.org/10.3390/en81112357

MULTIWALLED CARBON NANOTUBES-IMMOBILISED TANNASE FOR ENHANCEMENT OF *IN VITRO* ANTIOXIDANT ACTIVITIES OF GREEN TEA INFUSION

Chong-Boon Ong[1,2*] and Mohamad S. M. Annuar [2]

[1] *Faculty of Science, Technology, Engineering and Mathematics, International University of Malaya-Wales, City Campus, Jalan Tun Ismail, 50480 Kuala Lumpur.*
ongchongboon@iumw.edu.my

[2]*Institute of Biological Sciences, Faculty of Science, University of Malaya, 50603 Kuala Lumpur.*
suffian_annuar@um.edu.my

ABSTRACT

Owing to their remarkable mechanical stability, good dispersibility, high surface-to-volume ratio, and biocompatibility, carbon nanotubes (CNTs) are of special interest as matrix for immobilising enzymes. Therefore, immobilisation of glutaraldehyde cross-linked tannase on pristine multi-walled carbon nanotubes (MWCNT) was carried out. Immobilisation of tannase was accomplished by strong hydrophobic interaction, most likely between hydrophobic amino acid moieties of the cross-linked tannase to the MWCNT. The rate of DPPH˙ radical scavenging activities for tannase-treated green tea extract was shown to be higher than native green tea extract. MWCNT-immobilised tannase is a potential catalyst with high stability and excellent operational re-usability for biotransformation of catechins in green tea infusion. The improved antioxidant activities of green tea infusion extract can be exploited as dietary supplement in foods and beverages or in nutraceutical applications. Infusion preparation with elevated levels of antioxidants represents a source for extraction and purification at commercial scale.

Keywords: Tannase; Multi-walled carbon nanotubes (MWCNT); Immobilization; Antioxidants; Green tea

1. INTRODUCTION

Green tea (*Camellia sinensis*) is rich in polyphenols such as catechins or flavan-3-ols including epicatechin (EC), epigallocatechin (EGC), epicatechin gallate (ECG), and epigallocatechin gallate (EGCG), as well as the alkaloid, caffeine [1]. Polyphenols are the most abundant compounds in green tea extract and widely accepted as the major antioxidant in green tea. Tannase (or tannin acyl hydrolase, EC 3.1.1.20) has mostly been characterized by its hydrolysing activity on the ester bond (galloyl ester of an alcohol moiety) and the depside bond (galloyl ester of gallic acid) of substrates such as tannic acid, EGCG, ECG, and chlorogenic acid. It has many potential applications, among which the most important one is to catalyse the biotransformation of tea catechins, which increases their antioxidant activities [2].

The carbon nanotubes (CNTs) generally improves the efficiency of immobilised enzymes, because it provides a larger surface area for enzyme attachment, leading to higher enzyme loading per unit mass of particles [3]. Two main types of CNTs, single-walled carbon nanotubes (SWCNT) and multi-walled carbon nanotube (MWCNT), have been used to immobilise enzymes. However, MWCNT received greater attention due to their easy preparation, low cost, and excellent aqueous dispensability. In its free state, tannase has a high catalytic efficiency but there are some challenges to its commercial utilisation, including high cost of purified enzyme, its low stability during utilisation, and difficulties in recovering the enzyme for reuse. To overcome these challenges, enzyme immobilisation is often used in commercial applications to facilitate the handling, separation, reuse and stability of tannase. In the present work, glutaraldehyde-mediated cross-linked tannase *from Aspergillus ficuum* was immobilized by adsorption onto the pristine MWCNT. Post-immobilization structural changes of the preparation were analysed using spectroscopic and microscopic techniques. The study also investigated major catechins composition in tannase-treated green tea extract and compared its radical scavenging activities towards DPPH˙ free radical as a model system.

2. MATERIALS AND METHODS

2.1 Materials

Multiwalled carbon nanotubes (MWCNT; length of 3-6 μm and outer diameter of 10 nm ± 1 nm), tannic acid, gallic acid, rhodamine, glutaraldehyde solution, potassium hydroxide, and tannase from *Aspergillus ficuum* (EC 3.1.1.20; ≥150 U g^{-1}) were obtained from Sigma-Aldrich (St. Louis, MO, USA). Citric acid and trisodium citrate dihydrate were procured from Merck (Darmstadt, Hesse, Germany). Ultrapure water with 18.2 megaOhm cm^{-1} resistivity was used in preparing solutions.

2.2 Immobilization of tannase on MWCNT

One mg ml^{-1} of MWCNT was initially sonicated at 37 kHz frequency and 0.8 W (Elmasonic P30H, Elma, Singen, Germany) in 50 mM citrate buffer (pH 4.7) for 30 min to obtain a uniform dispersion. To the suspension, 1 mg ml^{-1} of tannase was added, and the mixture was shaken at 200 rpm for 30 min at room temperature (25 ± 1 °C). For cross-linking, 3 % (*v/v*) of glutaraldehyde was added to the solution and shaken at 200 rpm for 30 min at room temperature. After incubation, the immobilized tannase was separated by centrifugation (6153 × *g*, 30 min) and washed at least five times with fresh buffer.

2.3 Characterization of immobilised tannase

After immobilization, the sample was lyophilized using a ScanVac CoolSafe freeze-dryer machine (LaboGene, Lynge, Denmark). Fourier transform infrared (FTIR) analyses of pristine MWCNT, and tannase-immobilised MWCNT were performed on FT-IR Spectrum 400 spectrometer (Perkin Elmer, Waltham, USA). FTIR spectra was recorded in the frequency range of 4000 – 450 cm^{-1}, and the optical properties of the samples were identified using He-Ne (helium-neon) laser that emits red light at a wavelength of 633 nm. The morphologies of pristine MWCNT and tannase-immobilised MWCNT were observed under transmission electron microscope (TEM) Carl Zeiss LIBRA® 120 (Carl Zeiss, Oberkochen, Germany) operated at accelerating voltage of 120 kV. The individual sample (0.5 mg) of pristine MWCNT and enzyme-immobilized MWCNT were ultrasonicated (Elmasonic P30H, Elma, Singen, Germany) at 37 kHz frequency and 0.8 W for 15 min in deionized water. A drop of each sample was positioned on a copper grid and observed after drying in vacuum. Morphological observation for the pristine MWCNT and tannase-immobilized MWCNT was made under field emission scanning electron microscopy (FESEM) Quanta™ 450 FEG (FEI, Hillsboro, USA) operated at 10 kV.

2.4 Tannase assay

Tannase activity was determined by measuring the amount of gallic acid released from tannic acid [4].

2.5 Green tea extract preparation

A commercial green tea was bought from a local retail shop. Its infusion was prepared by mixing the samples (0.25 g) with 100 mL of ultrapure water preheated to 80 °C and incubated in a water bath at the same temperature for 5 min. The extract was cooled by means of immersion in an ice bath prior to filtration through Whatman filter paper No. 1 twice. Subsequently, the extract was freeze-dried using ScanVac CoolSafe freeze-dryer machine (LaboGene, Lynge, Denmark).

2.6 Enzymatic biotransformation

The lyophilised tea extract (1.0 mg) was dissolved in 1.0 mL of citrate buffer (pH 4.7, 50 mM) and incubated with 1.0 mg of free- and immobilised tannase for 30 min. The reaction mixtures were stirred at 200 rpm at 25 ± 1 °C. After 30 min, the reaction tubes were placed in an ice bath for 15 min

in order to constrain the progress of enzymatic reaction. A solution of pristine MWCNT (1 mg mL^{-1}) equivalent with the concentration of immobilised tannase support was used as control in the same buffer solution.

2.7 Determination of the Radical-scavenging Activity

2.7.1 DPPH Assay

Two hundred microlitre of samples or standard compounds, at various concentration (0.05 to 0.25 mg mL^{-1} or 0.05 to 0.25 mmol L^{-1}, respectively), were mixed to 3.8 mL of methanolic $DPPH^{\cdot}$ solution (0.1 mmol L^{-1}) in a disposable cuvette (1 cm × 1 cm × 4.5 cm) for 30 min at 25 °C in the dark. The absorbance was measured at 517 nm using JASCO V-630 Series spectrophotometer (Hachiōji, Tokyo, Japan) equipped with a temperature controller system (JASCO EHC-716). Results were displayed using JASCO Spectra Manager II version 2.10.01 (Hachiōji, Tokyo, Japan). The homogeneity of the reaction medium was provided by magnetic stirring at 800 rpm. For control, methanol was substituted for samples. The EC_{50} value was calculated by nonlinear regression analysis in GraphPad Prism® version 6.05 (La Jolla, CA, USA). EC_{50} value is defined as the amount of antioxidant needed to decrease the absorbance of $DPPH^{\cdot}$ by 50 % from the initial. Lower of EC_{50} value indicated a stronger antioxidant activity for a compound.

2.8 Statistical analysis

All experiments were performed as triplicates, and the values obtained were expressed as mean ± standard deviation (SD). *P* values < 0.05 were considered as statistically significant.

3. RESULTS AND DISCUSSION

3.1 Characterization of the MWCNT–tannase conjugates

3.1.1 Fourier transform infra-red spectroscopy (FTIR)

The resultant wave numbers of FTIR for the pristine MWCNT and tannase-immobilized MWCNT are presented in Table 1, respectively. Absorption peaks at different wavelengths include at 1599.86 cm^{-1} attributed to the graphite structure (C=C stretching associated with side wall defect) in MWCNT, and also peaks at 2853.92 cm^{-1} and 2924.93 cm^{-1} for asymmetric and symmetric C-H stretching bonds present in the structure of pristine MWCNT. The peaks at 3577.42 cm^{-1} and 3157.42 cm^{-1} encompassing a wide range of the spectrum pointed to the combination of stretching vibration of (N-H) and (O-H), which indicated the presence of tannase in the MWCNT. Furthermore, the presence of IR peak for nitriles (C≡N) at 2214.48 cm^{-1}, and aliphatic amide bond (C-N) at 1169.18 cm^{-1} further supported that the enzyme was successfully immobilized onto the MWCNT. In addition, peak at 1551.19 cm^{-1}, corresponding to the C=C stretching, MWCNT stretching aromatic mode, revealed that MWCNT retained its structure after immobilization.

Table 1. FTIR data for (a) pristine MWCNT, (b) tannase-immobilised MWCNT

	Frequency (cm^{-1})	Functional group
(a)	1575.47	C=C stretching
	2853.90, 2925.48	C-H stretching
	3450.60	O-H stretching
(b)	2218.59, 2214.65, 2229.61	Nitriles C≡N stretch
	1171.18	Aliphatic amines (C-N)
	3577.06	Amide N-H Stretch
	3178.29	Alcohol O-H Stretch
	1544.27	C=C stretching

3.1.2 Field Emission Scanning Electron Microscopy (FESEM) and Transmission Electron Microscopy (TEM) observation

The dimension and morphology of pristine MWCNT with and without the immobilized tannase were observed by FESEM and TEM at the same magnification. FESEM and TEM micrographs are shown in Figs. 1 and 2, respectively, for the pristine MWCNT (a) and immobilized tannase (b). As shown in Figs. 1(b) and 2(b), increased thickness dimension of the sidewall of the tannase-immobilized MWCNT compared to the pristine MWCNT (Figs. 1(a) and 2(a)) is a strong physical evidence of tannase deposition onto the surface of MWCNT and therefore, indicating successful immobilization of the enzyme onto MWCNT.

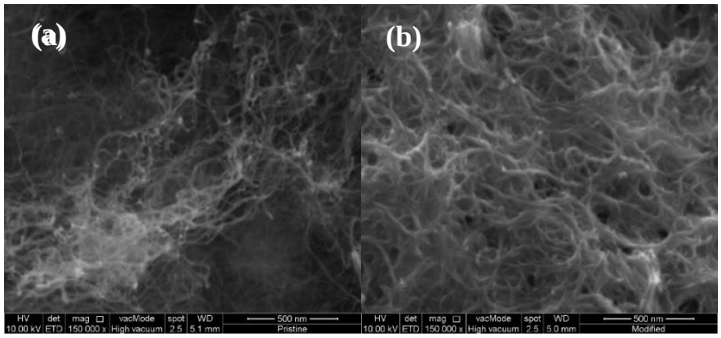

Figure 1 FESEM micrographs of **(a)** pristine MWCNT and **(b)** tannase immobilised onto MWCNT

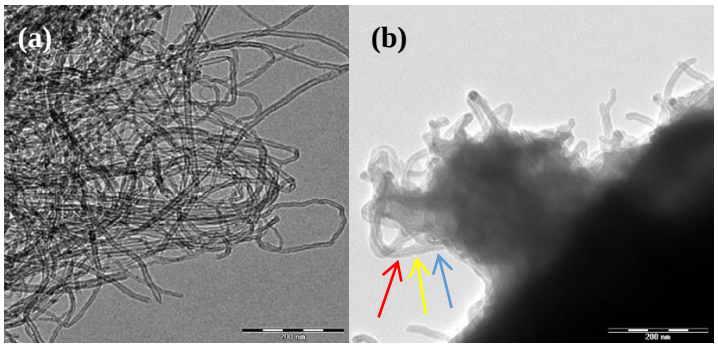

Figure 2 TEM micrographs of **(a)** pristine MWCNT and **(b)** tannase immobilised onto MWCNT. The arrows indicate the tannase immobilized on MWCNT surface

3.1.3 Antioxidant Activities of Green Tea Extracts

Tannase-treated green tea infusion extract exhibited higher DPPH˙ free radical-scavenging capacity than that observed for native green tea infusion extract ($p < 0.05$). The EC_{50} values determined for free tannase-treated green tea and immobilised-tannase treated green tea were 0.024 ± 0.001 mg mL^{-1} $mmol^{-1}$ DPPH and 0.032 ± 0.003 mg mL^{-1} $mmol^{-1}$ DPPH, respectively, while EC_{50} for native green tea infusion extract was found to be 0.044 ± 0.001 mg mL^{-1} $mmol^{-1}$ DPPH. The antioxidant activities of the green tea infusion extract increased by 39 % after enzymatic treatment.

4. CONCLUSION

Tannase was successfully immobilised onto dispersed MWCNT matrix as confirmed by FESEM, TEM, FTIR and enzyme activity analyses. Biotransformation of green tea extract for improved antioxidant activities can be achieved using immobilised tannase. The improved antioxidant activities of green tea infusion extract can be exploited as dietary supplement in foods and beverages or in nutraceutical applications. Enzyme-treated infusion offers a source for antioxidants extraction and purification at commercial scale.

REFERENCES

1 Williamson, G., Dionisi, F., Renouf, M., (2011). Flavanols from green tea and phenolic acids from coffee: Critical quantitative evaluation of the pharmacokinetic data in humans after consumption of single doses of beverages. Molecular Nutrition & Food Research, 55, 6, 864-873

2 Lu, M.J., Chen, C.S., (2007). Enzymatic tannase treatment of green tea increases *in vitro* inhibitory activity against *N*-nitrosation of dimethylamine. Process Biochemistry, 42, 9, 1285-1290

3 Li, Z.L., Cheng, L., Zhang, L.W., Liu, W., Ma, W.Q., Liu, L., (2017). Preparation of a novel multi-walled-carbon-nanotube/cordierite composite support and its immobilization effect on horseradish peroxidase. Process Safety and Environmental Protection, 107, 463-467

4 Sharma, S., Bhat, T.K., Dawra, R.K., (2000). A spectrophotometric method for assay of tannase using rhodanine. Analytical Biochemistry, 279, 1, 85-89

EXPERIMENTAL AND THEORETICAL STUDY OF ACOUSTIC CAVITATION WITH APPLICATION IN SOLID-LIQUID SEPARATION

Yijin Tan[1], Hiroya Muramatsu[2], Takayuki Saito[3]

[1]*Graduate school of Integrated Science and Technology, Shizuoka University*
tan.yi.jin.16@shizuok.ac.jp

[2]*Graduate school of Science and Technology, Shizuoka University*
muramatsu.hiroya.15@shizuoka.ac.jp

[3]*Research Institute of Green Science and Technology, Shizuoka University*
saito.takayuki@shizuoka.ac.jp

ABSTRACT

Recently, an innovative solid-liquid separation technique utilizing kHz-band ultrasound was introduced. This technique flocculates dispersed solid particles towards targeted location by inducing acoustic cavitation bubble. Compared to other separation techniques, this technique is non-contact and simple. In fact, this technique can be useful in pharmaceutical research such as the classification of encapsulated bioactive compound. However, the design of a unit operation based on this separation technique requires in-depth understanding and precise estimation of the phenomenon. Therefore, the present study aims to unravel the working principle of this separation technique. First, the formation, growth and motion of an acoustic bubble were visualized with high speed camera. Meanwhile, the levitation of a single polystyrene particle was also demonstrated. The results were used for the development of a simulation model that estimates the behavior of acoustic bubbles. With the help of the simulation model, chain-like flocculation pattern caused by CO_2 acoustic bubbles was explained. It was found that CO_2 bubble either dissolves away quickly or expands uncontrollably due to high solubility in water. These findings are useful for the design of a separator that classifies particle based on size.

Keywords: Ultrasound; Acoustic cavitation; Solid-liquid separation; Bjerknes force; Particle flocculation

1. INTRODUCTION

Solid classification by size can be useful in pharmaceutical research. For instant, particles produced from encapsulation of pharmaceutical chemical can be classified into different size ranges since particle size is a crucial parameter in defining product performance[1]. Encapsulation technologies are widely applied in the pharmaceutical industry due to its stability enhancement benefit. However, recent encapsulation strategies inevitably produce particles with size distribution[2]. Recently, an innovative solid-liquid separation technique utilizing kHz-band ultrasound was introduced. This technique flocculates dispersed solid particles towards targeted location by inducing acoustic cavitation bubble[3]. The potentials of this technique in solid classification based on size and in manipulation of flocculation position were also demonstrated. Compared to other separation techniques, this technique is non-contact and simple. However, the design of a unit operation based on this separation technique requires in-depth understanding and precise estimation of the phenomenon. Therefore, the present study aims to unravel the working principle of this separation technique. First, the formation and growth of an acoustic bubble from bubble nucleus to fragmentary acoustic bubble were visualized with high speed camera. Next, the radial and translational motions of a stable acoustic bubble attached on a solid particle were investigated. Finally, Muramatsu and Saito found that CO_2 bubble behaves differently in acoustic field compared to regular air bubble[4]. These behaviors were explained with the result of numerical analysis.

2. EXPERIMENTAL METHODOLOGY

2.1 Experimental Setup

Figure 1 shows the experimental setup for the generation and visualization of acoustic bubble. For the generation of ultrasound, 20kHz sine wave electrical signal was generated by a programmable function generator (SG-4105, Iwatsu) to be amplified by an amplifier (2100L, E&I). The amplified signal was converted into ultrasound by a bolt-clamped Langevin-type transducer (HEC-45254M, Honda Electronics). The transducer was bonded to a 3mm-thick stainless-steel plate that was set at the bottom of a levitation cell. The levitation cell was made from acrylic and the inner dimensions were 54mm×54mm as viewed from the top and the vessel was 150mm in height. The levitation cell did not have a base, in other words, the liquid in the levitation cell was in contact with the 3mm-thick stainless-steel plate. Purified but non-degassed water at 20°C filled the vessel, up to a depth of 60mm. The depth of water measure from the water is defined as the *z*-position. Along with the irradiation of ultrasound, acoustic bubble was generated. The free surface of the water acted as an ultrasound reflector to create standing wave in the levitation cell. In one of the experiments, the acoustic bubble was used to levitate a solid particle. The solid particle is made of polystyrene, spherically shaped with 1mm diameter and has a density of 1060kg/m^3. The motion of the acoustic bubble and the solid particle was recorded using highspeed camera (FASTCAM Mini AX200, Photron) through a long-distance microscope lens (CFV-4, Infinity) with halogen lamp (KTS-100RSV, Tokina) as backlight. The recorded images were processed with MATLAB R2015b.

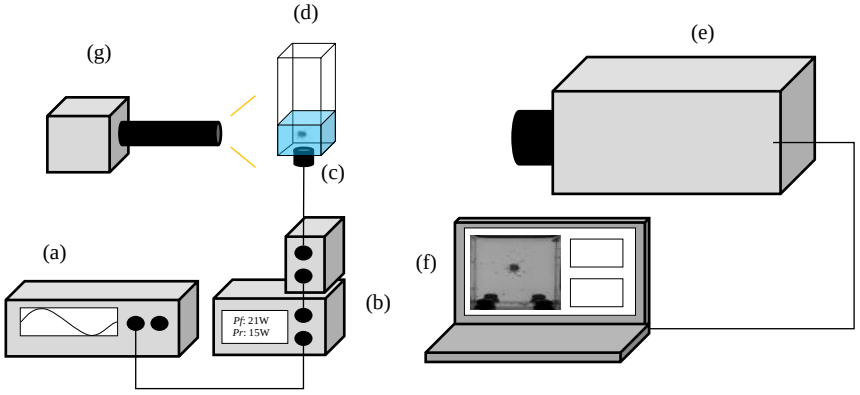

Figure 1. Experimental Setup for Acoustic Bubble Visualization. (a) Function Generator (b) Amplifier (c) Transducer (d) Levitation Cell (e) Highspeed Camera (f) Computer (g) Halogen Lamp.

2.2 Theoretical Models and Numerical Method

For deeper understanding of the phenomenon, the radial respond of an acoustic bubble was estimated with the Keller Miksis model[5] as shown below:

$$R\ddot{R}\left(1-\frac{\dot{R}}{c}\right)+\frac{3}{2}\dot{R}^2\left(1-\frac{\dot{R}}{3c}\right)=\frac{1}{\rho}\left(1+\frac{\dot{R}}{c}+\frac{R}{c}\frac{\mathrm{d}}{\mathrm{d}t}\right)\int_{P_\infty}^{P_L}\mathrm{d}P \quad \#(1)$$

$$\int_{P_\infty}^{P_L}\mathrm{d}P=\left(P_o+\frac{2\sigma}{R_0}-P_v\right)\left(\frac{R_o}{R}\right)^{3\kappa}+P_v-\frac{2\sigma}{R}-4\mu\frac{\dot{R}}{R}-P_0-P(t,z) \quad \#(2)$$

where R, c, ρ, t, P, subscript 0, σ, κ, P_v, μ and $P(t, z)$ are the bubble radius, speed of sound, water density, time, pressure in general, initial condition, polytropic index, surface tension, vapor pressure, water viscosity and acoustic pressure respectively.

Simultaneous to the bubble oscillation, the content of the bubble diffuses in or out of the bubble along the concentration gradient and this can be described as:

$$\frac{\mathrm{d}n}{\mathrm{d}t}=2\pi R^2 D(C_\infty-C_R)\left(\frac{1}{R}+\frac{1}{\sqrt{\pi Dt}}\right) \quad \#(3)$$

where n, D, C_∞ and C_R are number of moles of bubble content, gas diffusivity, concentration far from bubble and concentration in the bubble respectively. This causes the bubble to either grow by rectified diffusion or passively dissolves away. The equations were solved with the forth order RKF method to obtain R.

3. RESULTS AND DISCUSSION

Figure 2(a) shows photographs of the acoustic bubble oscillating under acoustic frequency (υ) of 20kHz and acoustic pressure (P) of 14.4kPa to 20.8kPa with a step change of 1.6kPa. The higher the acoustic pressure, the nearer the acoustic bubble is attracted towards the pressure antinode (i.e. 1.9mm below the bottommost of photograph). This is because as acoustic pressure increase, the pressure gradient experienced by the acoustic bubble increases, and so is the amplitude of bubble pulsation. Figure 2(b) shows the stationary position variation of the acoustic bubble as acoustic pressure was manipulated. The graph shows that the z-position is not linearly proportional to acoustic pressure. Instead, the change in z-position reduces as acoustic pressure increase. This is because pressure gradient varies with position in the standing wave. Although the pressure gradient at a fixed point is directly proportional to acoustic pressure, the pressure gradient reduced as the acoustic bubble approaches the pressure antinode (pressure gradient function is a cosine function with zero value at the antinode). Therefore, the acoustic bubble experiences less primary Bjerknes Force (attractive force) nearer to the antinode. The results were used to validate the simulation models used in the present study.

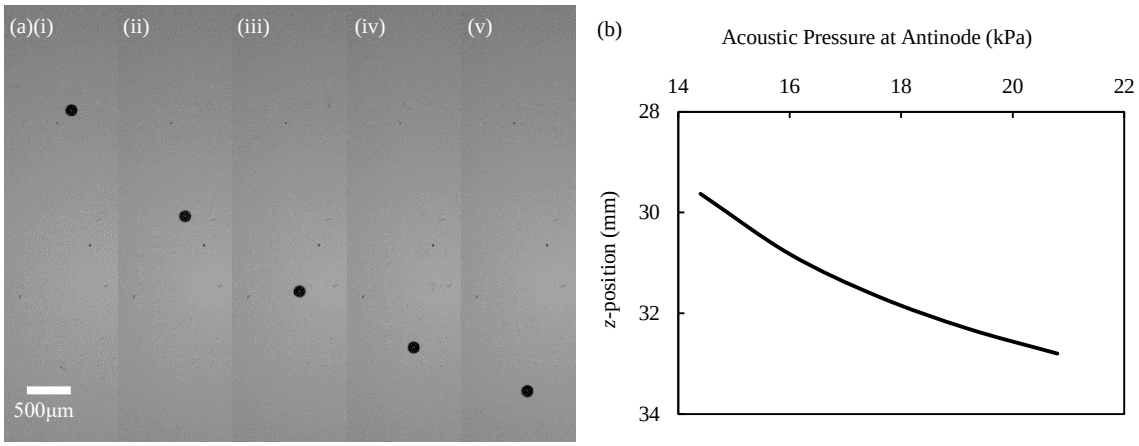

Figure 2. Stationary Position of the Acoustic Bubble with Varying Acoustic Pressure. υ = 20kHz; R_0 = 70.6μm (a) Selected Photographs of the Acoustic Bubble. P = 14.4~20.8kPa (b) Variation of Stationary Position against Acoustic Pressure.

By increasing the acoustic pressure to 80kPa, a fragmentary acoustic bubble was produce. It translates randomly (4mm displacement) around a mean position due to its irregular shape. When a solid particle was brought close enough to the acoustic bubble, the acoustic bubble attached to the solid and caused the solid particle to levitate around a mean position. Figure 3 shows consecutive photographs of a polystyrene particle levitated by an acoustic bubble. With the present of solid particle, the translational motion of the fragmentary acoustic bubble reduced due to the inertia of the solid particle making it difficult to accelerate, and due to the size of the solid particle which increased the drag force. As the result, the particle was levitated with displacement of less than 2mm around its mean position. This continued for the entire duration of ultrasound irradiation. The acoustic bubble stayed above the solid particle, implying that the acoustic bubble was supporting the polystyrene particle against sedimentation due to gravity. This agrees with the experimental analysis done by Mizushima[6] concluding that cavitation bubbles lead particles to flocculation position.

As an attempt to explain the differences in flocculation pattern found in air-dissolved water and CO_2-dissolved water[4], the bubble behavior was analyzed using the simulation model validated in the present study. Figure 4(a) shows the change in equilibrium bubble radius of an air bubble and a CO_2

bubble under 40kPa acoustic pressure. It was found that CO_2 bubble dissolves away passively due to high solubility in water compared to air bubble which mainly contain nitrogen and oxygen. Small number of functionable acoustic bubbles results in inability to form large spherical flocculation, but still capable to flocculate in a chain-like manner. On the other hand, figure 4(b) shows the change in equilibrium bubble radius of CO_2 bubble under 70kPa acoustic pressure in CO_2-dissolved water of different concentrations. It was found that high concentration of CO_2 causes bubble to grow rapidly (0.8% increment in 10 acoustic cycles). This bubble will eventually rise when the buoyancy force outweighs the primary Bjerknes force. Moreover, an acoustic bubble larger than the resonance size will be repelled from the flocculation position. This agrees with the findings reported by Muramatsu and Saito[4].

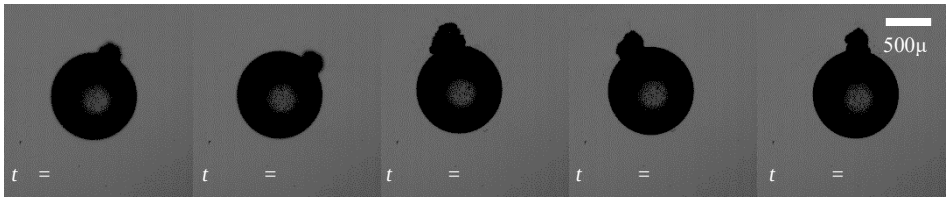

Figure 3. Consecutive Photographs of a Ø1mm Polystyrene Particle (Large Circle) Levitated with an Acoustic Bubble (Irregularly Shaped Object Attached on The Particle). P = 80kPa; υ = 20kHz

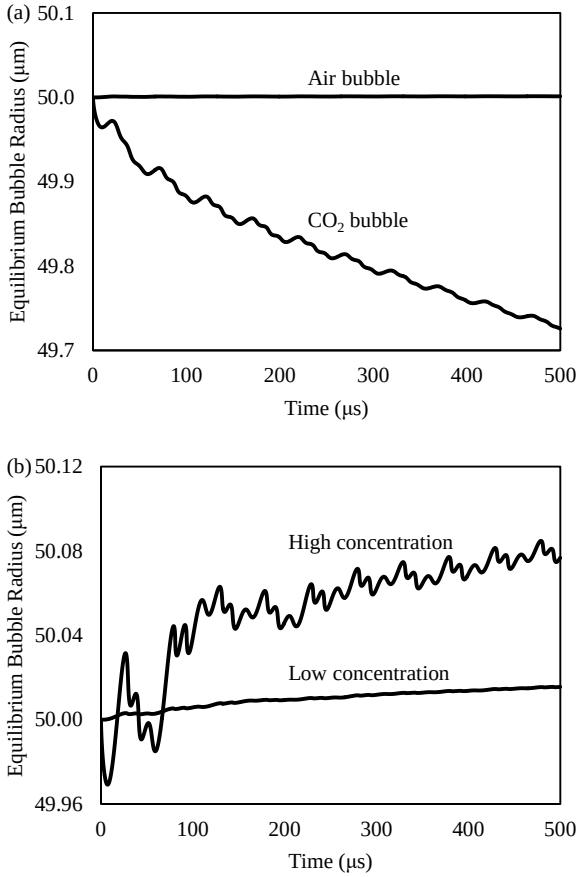

Figure 4. Change in Equilibrium Bubble Radius against Time. (a) Air Bubble versus CO_2 Bubble. (b) CO_2 Bubble in 20.7M/m^3 CO_2-dissolved water versus 28.9M/m^3 CO_2-dissolved water.

4. CONCLUSION

In the present study, the mechanism of a novel separation technique using ultrasound was visualized. The result was used to develop a simulation model that predicts acoustic bubble behavior. Different flocculation patterns were also discussed and explained using the simulation model. As future work,

the simulation model will be further improved to estimate the phenomenon with higher accuracy and reliability.

REFERENCES

1. Mancer, D., Allemann, E. , Daoud, K., (2018). Metformin hydrochloride microencapsulation by complex coacervation: Study of size distribution and encapsulation yield using response surface methodology, J. Drug Deliv. Sci. Technol., 45, 184–195
2. Rodríguez, J., Martín, M. J., Ruiz, M. A., Clares, B., (2016). Current encapsulation strategies for bioactive oils: From alimentary to pharmaceutical perspectives, Food Res. Int., 83, 41–59
3. Muramatsu, H., Saito, T., (2018). An innovative unit operation of particle separation/classification by irradiating low-frequency ultrasound into water, AIChE J., 64, 5, 1564–1572
4. Muramatsu, H., Saito, T., (2017). The relationship between bubble motion and particle flocculation pattern under 20-kHz-ultrasound radiation in water, Chem. Eng. Sci., 170, 195–203
5. Keller, J. B., (1980). Bubble Oscillations of Large Amplitude, J. Acoust. Soc. Am. - J ACOUST SOC AMER, 68, 628-633
6. Mizushima, Y., Nagami, Y., Nakamura, Y., Saito, T., (2013). Interaction between acoustic cavitation bubbles and dispersed particles in a kHz-order-ultrasound-irradiated water, Chem. Eng. Sci., 93, 395–400

DEVELOPMENT OF A SIMULTANEOUS MEASUREMENT TECHNIQUE FOR DENSE-FOAM CELL SIZE AND FILM THICKNESS, BY USING A SINGLE-TIP OPTICAL FIBER PROBE

Hiroya M. Mizutani[1, *] and Takayuki Saito[2]

[1]*Graduate school of Science and Technology, Shizuoka University, 3-5-1 Johoku, Naka-ku, Hamamatsu, Shizuoka 4328561, Japan*
muramatsu.hiroya.15@shizuoka.ac.jp

[2]*Research Institute of Green Science and Technology, Shizuoka University, 3-5-1 Johoku, Naka-ku, Hamamatsu, Shizuoka 4328561, Japan*
saito.takayuki@shizuoka.ac.jp

ABSTRACT

Foam is frequently encountered in industrial fields (e.g., chemical plant and floatation process) and our daily life (e.g., soap and fresh cream). An optical fiber probing (OFP) method has the potential to simultaneously measure both the cell size and cell film thickness. In the present study, we aim to discuss the measurement mechanisms and performance of this technique numerically and experimentally. First, we experimentally investigated film-thickness measurement by piercing a simulated thin liquid film. Second, we numerically investigated optical signals from the corresponding optical system by using our original three-dimensional ray tracing method. By comparing both results, we succeeded in clarifying the physical meanings of the optical signals. In this film thickness measurement, the difference between the OFP measurement and mass-based measurement was -15 to +30 %. Third, we measured real foam cell size by penetrating the S-TOP into the foam cluster. In the cell size measurement, the difference between the OFP measurement and visualization was less than 10 %. Finally, we concluded that our OFP measurement technique can be practically used for dense foam measurement.

Keywords: Optical fiber probe; Dense foam; Measurement technique; Visualization; Numerical simulation

1. INTRODUCTION

Foam, one of the gas-liquid dispersion phases, is frequently encountered not only in industrial fields (e.g., chemical plant and flotation process) but also in our daily life (e.g., soap and fresh cream). Controlling the foam formation or characteristics provides improving the efficiency of equipment and safety in industrial fields for us. Thus, many researchers have been devoting themselves to development of the foam measurement techniques such as electrical conductivity method [1] and image processing method [2, 3]. The former one has an advantage of measuring the average foam cell size in a vessel. The latter one can measure size of the cells which adhere to the transparent vessel wall. However, these measurement techniques provide us only the cell size, but cell film thickness measurement is impossible. We have been developing optical fiber probing (OFP) method which is able to measure bubble/droplet chord length, velocity, void fraction, surface tension etc. [4-6]. The OFP method has the potential to simultaneously measure both foam cell properties (i.e., cell size and film thickness). The purpose of the present study is to investigate the measurement mechanisms and performance of this new foam measurement technique, numerically and experimentally. First, we experimentally investigated film thickness measurement by means of OFP's piercing a simulated thin liquid film. Second, we numerically investigated optical signals from the corresponding optical system by using our original three-dimensional ray tracing simulation. By comparing both obtained results, we revealed the physical meanings of the complex optical signals. Third, we measured real foam cell size and cell thickness by penetrating foam clusters, with visualization for reference. We discussed the practical use of our OFP measurement technique in the field of dense foam measurement.

2. OPTICAL FIBER PROBING METHOD

In the present study, we employed a single tip optical fiber probe (S-TOP) for dense foam measurement. The principle of the OFP method utilizes the difference in refractive indices between the optical fiber and the liquid/gas phase. Fig. 1 shows the optics of this OFP measurement. The optics consists of a laser diode (wavelength: 635nm, Polarization: linear, Edmund Optics), a beam splitter (CSMH-10-550, Sigmakoki), an objective lens (OBL-40, Sigmakoki), a polarizer (SPF-30C-32, Sigmakoki), a photomultiplier tube (R928, Hamamatsu), an amplifier (C7319, Hamamatsu), and a digital recorder (8861-50 & 8965, Hioki). The laser beams from the laser diode were entered into the incident tip of the S-TOP through the beam splitter and objective lens. The beams were propagated in the S-TOP. The beams reflected at the sensing tip were entered in the PMT through the polarizer. The PMT signal was amplified by the amplifier, and stored in the digital recorder. When the sensing tip was positioned at a gas phase, the most of beams were reflected at the sensing tip. Hence, the PMT output signal was high. On the other hand, when the sensing tip was positioned at a liquid phase, beams are discharged into the liquid phase. The output signal was low. From the variation of the output signal, the film thickness and cell size are measured.

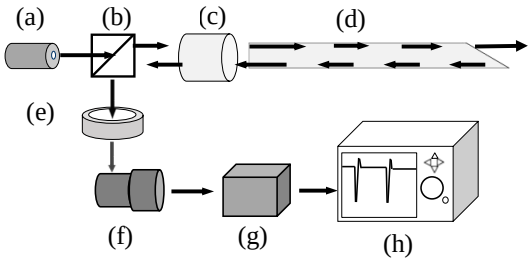

Figure 1. Optics of optical fiber probing method. (a) Laser diode, (b) Beam splitter, (c) Objective lens, (d) S-TOP, (e) Polarizer, (f) Photomultiplier tube, (g) Amplifier, (h) Digital recorder.

3. METHOD

3.1. Film Thickness Measurement

A schematic diagram of the liquid film thickness measurement used in the present study is illustrated in Fig. 2. The S-TOP was mounted on an automatic stage (Stage: SGSP20-85, Controller: PAT-001, Sigma Koki). The S-TOP was downwardly moved into the liquid film, and the stage velocity was set at 4 mm/s. To prevent burst of the liquid film, we used a water-based solution made from water, polyvinyl alcohol and neutral detergent (mass ratio of 20:20:1, density: 0.9285 g/cm^3, refractive index: 1.333). In this film thickness measurement, since it was difficult to measure a film thickness by visualization, the average film thickness was estimated from the mass of the liquid film. In the cell size measurement, the cell size was measured by a high-speed camera.

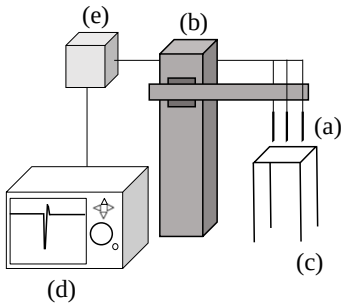

Figure 2. Experimental setup for liquid film measurement. (a) S-TOP, (b) automatic stage, (c) liquid film stand, (d) Digital recorder, (e) Optics.

3.2. Numerical Simulation

We employed the three-dimensional ray tracing simulator which was developed by Sakamoto and Saito [7]. This numerical simulator was composed of “Surface”, “Body” and “Ray”. The rays (: members of the Ray) were reflected, refracted and transmitted at cross-points of the surfaces (: members of the Surface) and the rays. The directions of the ray segments were calculated by Snell’s law. In addition, the reflectivity and transmissivity were calculated by Fresnel’s law. In order to investigate the physical meanings of the output signal, we classified the signal into 5 groups; (1) Energy of ray reflected at the sensing tip (E_s), (2) Energy of ray reflected at the frontal interface of the thin film (E_f), (3) Energy of ray reflected at the rear interface of the thin film (E_r), (4) Energy of the ray reflected at the meniscus in the frontal interface of the thin film (E_{fm}) and (5) Energy of the ray reflected at the meniscus in the rear interface of the thin film (E_{rm}).

4. RESULTS AND DISCUSSIONS

Figure 3 shows a typical experimental result obtained from a pair of thin liquid films penetrated by the S-TOP. When the S-TOP touched the film, the output signal dropped (Red arrows in Fig. 3 (a)), rapidly. After the S-TOP sensing-tip's penetrating the first film, the S-TOP’s sensing tip was exposed to the air, the signal was thus increased. T The cell size was calculated from the S-TOP's velocity multiplied by the time interval Δt. The difference between the visualization and S-TOP in the distance measurement of the parallel thin films was less than 2%.

Figure 3 (b) shows the enlarged signal of the same section in time scale from 2.82 sec to 2.92 sec of Figure 3 (a). The local maximum value is observed; a gray arrow marks it in Figure 3 (b). So far, the important signal for measuring the film thickness is not appearing explicitly. Figure 4 shows typical numerical simulation result. The shape of the total energy E_t (black line) is similar to the experimental result. By careful observation of the decomposition signals, E_f and E_{fm} are negligibly small during the penetration process. Before touching the film, the high-level signal is composed of E_s. When the S-TOP starts piercing the film, E_s ($\approx E_t$) decreases. The delay of the dropping signal is caused by the S-TOP’s geometric structure (i.e., the gap between the S-TOP’s sensing edge and sensing area (see Figure 4(b)). On the other hand, E_r is gradually increasing. When the S-TOP’s sensing edge touches the rear interface of film, E_r reaches the maximum value. After that, the meniscus at the rear interface is formed and E_{rm} is gradually increasing. In addition, the S-TOP’s sensing edge starts exposing to the gas phase, and E_s is increasing. On the basis of this result, the local maximum value in Figure 3 (b) expressed the timing in which the S-TOP touched the rear interface.

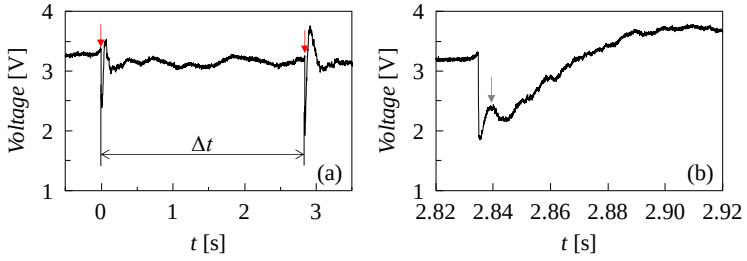

Figure 3. Experimental result of a pair of film penetration. (a) output voltage through the parallel films penetration. (b) enlarged signal in which S-TOP penetrated the rear film.

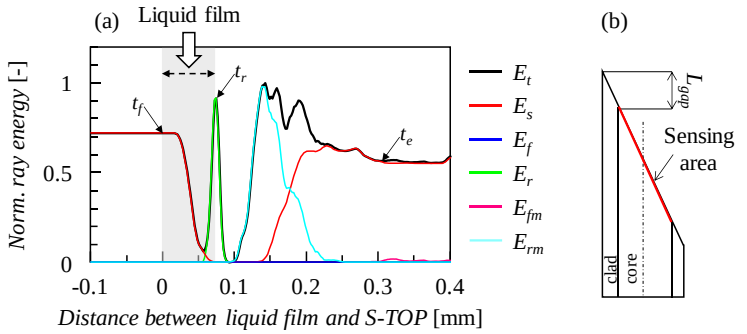

Figure 4. A typical numerical simulation result. (film thickness = 70 μm, OFP diameter = 140 μm). (a) t_f: time in which the S-TOP touched the frontal interface. t_r: time in which the S-TOP touched the rear interface. t_e: time in which the S-TOP's sensing area finished penetrating the film. (b) geometric structure of the S-TOP.

The film thickness measurement results are summarized in Table 1. The difference between the S-TOP measurement and mass-based measurement was from -15 % to + 30 %. In the light of the measurement principle, the film thickness has to be larger than the S-TOP's sensitive length.

Table 1. Comparison of the film thickness measurement

S-TOP measurement [μm]	Mass-based measurement [μm]	Difference [%]
24.0	22.6	-5.65
24.0	25.6	6.33
24.7	27.6	11.8
33.1	26.5	24.8

Figure 5 shows the experimental results of cell size measurement in a foam cluster. From the visualization result, the mean diameter of the cell cluster was estimated at 3.27 mm. By increasing the number of trials, the standard error was decreased. The difference between the visualization and the OFP measurement was -8.89 %. This difference was caused by the piercing position of the cells.

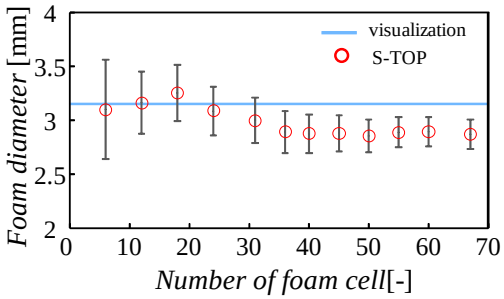

Figure 5. Cell size measurement results in a foam cluster.

5. CONCLUSIONS

We aimed at developing a novel foam measurement technique and investigating its performance. By comparing the experimental results and numerical results, we were able to extract the physically meaningful signals. We succeeded in the use of our OFP measurement technique for dense foam measurement. In future, we improve the S-TOP performance in dense foam measurement by using another original probe (i.e., fs-probe [4]).

REFERENCES

[1] Xie, W., Neethlin, S.J., Cilliers, J.J., (2004). A novel approach for estimating the average bubble size for foams flowing in vertical columns, Chemical Engineering Science, 59, 81-86.

[2] Lu, K., Li, R., Wu, Z., Hou, K., Du, X., Zhao, Y., (2013). Wall effect on rising foam drainage and its application to foam, Separation and Purification Technology, 118, 710-715.
[3] Carey, E., Stubenrauch, C., (2013). Free drainage of aqueous foams stabilized by mixtures of a non-ionic (C12DMPO) and an ionic (C12TAB) surfactant, Colloids and Surfaces A: Physicochemical and Engineering Aspects, 419, 7-14.
[4] Saito, T., Matsuda, K., Ozawa, Y., Oishi, S, Aoshima, S., (2009). Measurement of tiny droplets using a newly developed optical fibre probe micro-fabricated by a femtosecond pulse laser, Measurement Science and Technology, 20, 114002.
[5] Higuchi, H., Saito, T., (2010). Quantitative characterizations of long-period fluctuations in a large-diameter bubble column based on point-wise void fraction measurements, Chemical Engineering Journal, 160, 284-292.
[6] Mizushima, Y., Saito, T., (2012). Detection method of a position pierced by a single-tip optical fibre probe in bubble measurement, Measurement Science and Technology, 23, 085305.
[7] Sakamoto, A., Saito, T., (2012). Computational analysis of responses of a wedge-shaped-tip optical fiber probe in bubble measurement, Review of Scientific Instruments, 83, 075107.

INFLUENCE OF NUTRIENT MANAGEMENT ON CROP YIELD IN POLYCULTURE SYSTEM

Norfakhrina Mohd Noor, Nur Amalina Mohd Ropi, Ong Pei Ying, Muhamad Helmi bin Nadri, Cheng Kian Kai and Leong Hong Yeng*

Innovation Centre in Agritechnology, Universiti Teknologi Malaysia, 84600 Pagoh, Johor, Malaysia for Advanced Bioprocessing

*norfakhrina@utm.my, nuramalina.mr@utm.my, o.peiying@utm.my, muhammad.helmi@utm.my, chengkiankai@utm.my, *hongyeng@utm.my*

ABSTRACT

Increasing food demand due to higher population, urbanization and competition for land resulted in intensive farming practices to increase yield per area. It is essential to adopt sustainable agricultural practices that are sociable viable and environmental sound to maintain productivity and in the same time conserve resources. The main objective of this study is to determine the influences of different types of fertilizer towards crop yield in polyculture system. This study including application of organic fertilizer, inorganic fertilizer, organic-inorganic compound fertilizer and organic+inorganic fertilizer toward polyculture crop. Integration of organic and inorganic fertilizer showed better result to increase crop yields. Thus, plant needs organic and inorganic fertilizer to increase fertilizer efficiency and produce high yield of production.

Keywords: Polyculture crop; yield; organic fertilizer; bio-fertilizer; inorganic fertilizer

1. INTRODUCTION

Increased in human population has led to higher demand for food production globally. In the same time urbanization and competition for land have also resulted in intensive farming practices to increase yield per area through higher nutrient and water inputs [1]. Intensive agriculture activities often associate with significant environmental impact such as deforestation, pollution, greenhouse gas emission, soil quality change and reduction of biological activity which has compromised food production, environment and social safety [2,3]. Sustainable farming system aims to maintain the productivity via conservation of resource to ensure it is social viable and environmental sound [4]. Sustainability of agricultural activities until now is still a debating issues. Disregards whether is organic farm or conventional farm, overall management determines the sustainability of a farming system [5]. Sustainable farming system is the key to ensure the future of agriculture and food production. Nowadays, demand for organic foods is increasing especially among the health conscious consumers. Awareness of food superiority which are good for health and environment become the priority for people. Furthermore, consumers often look upon the taste and healthiness of organic products [6]. Growth and yield of vegetable crops are mainly depending on the quality and quantity of fertilizers used [7]. One of the major problems limiting crop production is soil fertility [8]. Inorganic fertilizer is often used to increase the soil fertility and crop yield. Alteration of texture and physical property of soil is always associate with frequent and high application rate of inorganic fertilizer. Moreover, the nutritional value of crops will be affected seriously by the continuous use of inorganic fertilizer [9]. Therefore, this research aims to assess the influence of organic fertilizer, inorganic fertilizer and organic-inorganic compound fertilizer toward yield of crops.

2. MATERIALS AND METHODS

2.1. Cultivar Selection and Seed Materials

Seeds of Water spinach, *Ipomoea aquatica*; Okra, *Hisbiscus esculentus*; and Dwarf Yardlong Bean, *Vigna unguiculata* var *sesquipedalis* were sown in seed trays (5cm-diameter) containing peatmoss. After emergence, the seedlings were transplant to soil beds

2.2. Study Site

Field experiment was conducted at research farm of Universiti Teknologi Malaysia Pagoh (UTM-Pagoh) for 12 weeks.

2.3. Experimental Design

Three type of plants (Water spinach, *Ipomoea aquatica*; Okra, *Hisbiscus esculentus*; and Dwarf Yardlong Bean Dwarf yardlong bean, *Vigna unguiculata*) were polycultured on soil bed (1m X 4m). Five different treatments of fertilizer were applied, T1: control treatment without fertilizer input; T2: organic fertilizer (Midori 3:3:3), T3: inorganic fertilizer (YaraMila 16:16:16), T4: organic–inorganic compound fertilizer (Midori 6:6:6), T5: organic + inorganic fertilizer (Midori 3:3:3 + YaraMila 16:16:16). Fertilizer were applied at first, second, sixth and tenth week after planting according nutrient requirement of plant as per recommendation from Department of Agriculture Pulau Pinang [10]. Experiment was a completely randomized block design with three replications per treatments.

2.4. Measurement of Yield Parameter

Water spinach were harvested after a month of planting. Fruits of okra and Dwarf Yardlong Bean were ready for harvesting 1.5 months after planting. The harvesting was done every 2-3 days when the okra fruits was 5- 6 inches with bright-green colour and the Dwarf Yardlong Bean Dwarf yardlong beanpods were well-filled out with seeds and the colour was bright green.

2.5 Statistical Analysis

The results were evaluated with analysis of variance (ANOVA) and Duncan's Multiple Range test (DMRT) procedures of the Statistical Packages for Social Sciences (SPSS). Means comparisons between treatments were performed by least significant different (LSD) test at $p<0.05$.

3. RESULTS AND DISCUSSION

Table 1. Yield of crops based on different fertilizer treatment

	Treatment	Water spinach	Dwarf Yardlong Bean	Okra
T1	No fertilizer	49.40 ± 6.39^{c}	72.57 ± 34.69^{a}	156.15 ± 39.55^{b}
T2	Organic fertilizer	62.61 ± 12.94^{abc}	53.66 ± 5.24^{a}	149.70 ± 22.72^{b}
T3	Inorganic fertilizer	87.62 ± 19.46^{a}	39.32 ± 16.84^{a}	178.42 ± 35.12^{b}
T4	Organic–inorganic compound fertilizer	55.56 ± 13.98^{bc}	39.39 ± 16.24^{a}	126.41 ± 18.04^{b}
T5	Organic+inorganic fertilizer	75.92 ± 10.33^{ab}	36.74 ± 15.51^{a}	300.14 ± 115.08^{a}

Mean ± s.d followed by different letters in the same column are statistically different according to Duncan's multiple range test $p<0.05$

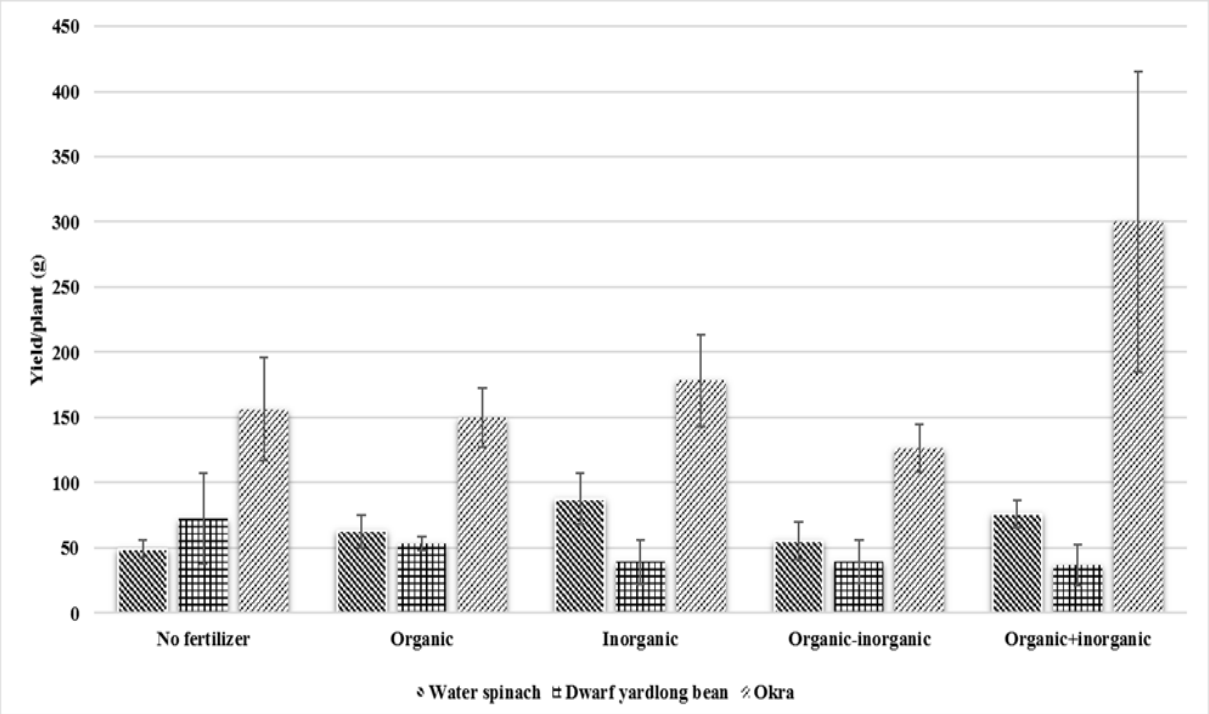

Figure 1. Graph yield crops based on different fertilizer treatment

Table 1 showed the yield of crops based on different fertilizer treatment. Yield of crops greatly influenced by fertilizer application. There was a highly significant different ($p<0.05$) among the yield of water spinach. Application of inorganic fertilizer to water spinach resulted the highest yield (87.62 ± 19.46 g/plant) and had significant difference ($p<0.05$) compared to application of organic–inorganic compound fertilizer (55.56 ± 13.98 g/plant) and without fertilizer (49.40 ± 6.39 g/plant). However, no significant difference ($p>0.05$) as compared to organic fertilizer (62.61 ± 12.94 g/plant) and organic+inorganic fertilizer (75.92 ± 10.33 g/plant). Similarly, yield of okra showed significantly difference ($p<0.05$) among the treatment. Application of organic+inorganic fertilizer (300.14 ± 115.08 g/plant) on okra yielded the most significant difference compared to other fertilizer application. However, dwarf yardlong bean had no significant difference ($p>0.05$) among treatment. Practice of intercropping often associated with organic farming. Family of legumes as bean have been encouraged to be planted for organic intercropping crops [11]. For some plants, organic fertilizers were sufficient to encourage the capability of plants to produce high total yield [8]. Conversely, input of organic and inorganic fertilizer together to the crops balanced the quantity of nutrient requirement needs for crops [12]. Addition of suitable organic fertilizer to the soil improves soil physical and chemical properties which encourages better root development, increased nutrient uptake and water holding capacity which leads higher crop yield and better fruit quality [13]. Moreover, application of organics in crop could improve synchronization of nutrient release and enhanced efficiency of chemical fertilizer [14]. Therefore, integration of organic and inorganic fertilizer could be considered as a better option in increasing fertilizer use efficiency and providing a more balanced supply of nutrients.

4. CONCLUSION

In conclusion, the best yield of crop could be obtained with application of integration organic and inorganic fertilizer. Based on the data, use of fertilizer combination organic and inorganic could be recommended to the farm management to produce better yield for polyculture system.

ACKNOWLEDGEMENT

The authors express their sincere thanks to Universiti Teknologi Malaysia for financial support (GUP grant: Q.K130000.2609.15J18, reference no: PY/2017/01638). Special thanks to Zenxin Agriculture Sdn. Bhd. for sponsoring research materials for this research.

REFERENCES

1. Foley J. A., De Fries, R., Asner, G. P., Barford, C., Bonan, G., Carpenter, S. R., Chapin, F. S., Coe, M.T., Daily, G. C., Gibbs, H. K., Helkowski, J. H., Holloway, T., Howar, E. A., Kucharik, C. J., Monfreda, C., Patz, J. A., Prentice, I. C., Ramankutty, N., Synder, P. K. (2005). Global consequence of land use, Science, 309, 5734, 570-574.
2. FAO, (2015). The Post-2015 Development Agenda and the Millennium Development Goals. Rome, Italy Food and Agriculture Organization of the United Nations (FAO).
3. Stoate, C., Boatman, N. D., Borralho, R. J., Carvalho, C. R., Snoo, G. R. d., & Eden, P. (2001). Ecological impacts of arable intensification in Europe. Journal of Environmental Management, 63, 4, 337-365.
4. Rigby, D., Cáceres, D. (2001). Organic farming and the sustainability of agricultural systems. Agricultural Systems, 68, 1, 21-40.
5. Hong Yeng, L., Agamuthu, P. (2015). Nitrogen flow in organic and conventional vegetable farming systems: a case study of Malaysia. Nutrient Cycling in Agroecosystems, 103, 2, 131-151.
6. Ekelund, L., Tjärnemo, H. (2004). Consumer preferences for organic vegetables- The case of Sweden. Acta Horticulturae, 665, 121-128.
7. Chang, K. H., Wu, R. Y., Chuang, K. C., Hsieh, T. F., Chung, R. S. (2010). Effect of chemical and organic fertilizers on growth, flower quality and nutrient uptake of *Anthurium andreanum*, cultivated for cut flower production. Scientia Horticulturae, 125, 434-441.
8. Kalbani, F.O.S.A., Saleem, M. A., Cheruth A. J., Kurup, S. S., Senthilkumar, A. (2016). Effect some organic fertilizers on growth, yield and quality of tomato (*Solanum lycopersicum*). International Lettrers of Natural Sciences, 53, 1-9.
9. Shimbo, S., Zhang, Z. W., Watanabe, T., Nakatsuka, H., Matsuda-Inoguch, N., Higashikawa, K., Ikeda, M. (2001). Cadmium and lead contents in rice and other ceral products in Japan in 1998-2000. Science of the Total Environment, 281,165-175.
10. DOA, 2018. Bendi. JABATAN PERTANIAN PULAU PINANG, Pulau Pinang
11. Peksen, E., Gulumser, A. (2013). Intercropping efficiency and yields of intercropped maize (*Zea mays* L.) and dwarf bean (*Phaseolus vulgaris* L.) affected by planting arrangements, planting rates and relative time of sowing. Internationa Journal of current Microbiology and Applied Sciencee, 2, 11, 290-299.
12. Suge, J. K., Omunyin, M. E., Omami, E. N. (2011). Effect of organic and inorganic sources of fertilizer on growth, yield and fruit quality of eggplant (*Solanum Melongena L*), Archives of Applied Science Research, 3, 6, 470-479.
13. Agbede, T. M., Ojeniyi, S. O., Adeyemo, A. J. (2008). American-Eurasian Journal Sustainable Agriculture, 2, 72–77.
14. Esilaba, A. O., Byalebek, J. B., Delve, R. J., Okalebo, J. R., Senyange, D. Mbalule, M., Ssali, H., (2005). Agricultural Systems, 86,144-165

EFFECT OF MICROWAVE SELECTED PARAMETERS ON PROPERTIES OF SYNTHESIZED MAGHEMITE FOR LIPASE IMMOBILIZATION

Ariffin, M.F.K[1*] and Idris, Ani[2]

[1]*Institute of Bioproduct Development, Faculty of Chemical and Energy Engineering, Universiti Teknologi Malaysia, 81310 UTM Johor Bahru, Johor, Malaysia*
maryamfarhana5@gmail.com

[2]*Institute of Bioproduct Development, Faculty of Chemical and Energy Engineering, Universiti Teknologi Malaysia, 81310 UTM Johor Bahru, Johor, Malaysia*
ani@cheme.utm.my

ABSTRACT

Maghemite nanomagnetic was successfully synthesized using microwave assisted technique. The working time for synthesis was shortened to 18 minutes using microwave compared with 7 hours conventionally. The amount of product formed was recorded at 0.362g (microwave condition: 80℃, 18 min and 300 MHz.) Produced maghemite showed superparamagnetic properties with good saturation magnetization recorded at 60.1 emu. The average size for synthesized maghemite was ~15 nm and in spherical shape based on FESEM analysis. Dielectro scanning calorimetry analysis showed that the maghemite undergoes phase change at ~450 ℃. Synthesized maghemite was applied as the carrier for lipase immobilization. The nanomaterial was coated with chitosan to assist amine linkage of lipase enzyme to the maghemite matrix. Immobilization process was conducted in thermal shaking incubator at 55 ℃, 200 RPM shaking speed and 9 hours incubation time. Immobilized lipase activity was evaluated through hydrolysis of *p*-nitrophenyl palmitate and measured using UV-vis spectrophotometer at 410 nm. The recorded lipase activity was 1.8 U.

Keywords: Microwave synthesis; maghemite; lipase immobilization

1. INTRODUCTION

Microwave (MW) irradiation is currently one of the fast emerging techniques in material syntheses. The method allows reaction to proceed at significantly reduced time, better product specificity and environmental friendly. Energy is supplied to the polar materials *via* dielectric heating which occurs inline as molecular dipoles align with the alternating electric field (Osborne *et al.*, 2012). The process creates thermal energy faster than conventional convection heating (Hu *et al.*, 2011). In this research, MW assisted technique has been exploited to synthesize maghemite nanomagnetic materials. The process produced maghemite at significantly reduced time as only 20 minutes is required for process completion. Due to the nano-sized and bio-compatibility of maghemite, the material has attracted interest to be manipulated as lipase immobilization matrix. Small size of maghemite allows shorter substrate diffusional path and large surface area available for lipase immobilization (Kim *et al.*, 2005). To cater such function, maghemite undergoes chitosan/glutaraldehyde treatment to assist amine linkage onto maghemite. Presence of chitosan in the immobilization complex prevents significant enzyme activity loss. The immobilized lipase activity showed only 20% activity reduction post hydrolysis reaction. Such stability creates good immobilized lipase enzyme (Chiou and Wu, 2004; Romdhane, Romdhane and Gargouri, 2011). Lipase (E.C 3.1.1.3) is widely known for its interfacial hydrolytic activity. The enzyme hydrolyses triacylglyceride complex to simpler molecules; fatty acids and glycerol. Lipases in their native form (free enzyme) creates many drawbacks when utilize in biocatalysis. For instance, the enzyme recovery in the downstream processing post- reactions is laborious and not efficient. By immobilizing the enzyme, catalyst separation from reaction mixture is simplified. In this study, when lipase is immobilized onto nanomagnetic nanoparticles; maghemite, introduction of external magnet able to separate the enzymes from mixture without any further treatments. The ability of lipase to work in wide range of environments and its ability to switch its function from a hydrolase to an esterase depending on the working medium further enhance the enzyme's exploitation in the world of synthesis.

2. METHODOLOGY

2.1 Maghemite Nanoparticle Synthesis

$FeCl_3.6H_2O$, $FeCl_2.4H_2O$ and $Fe(NO_3)_3$ were purchased from Sigma-Aldrich (M) and used without further treatment. Hydrochloric acid, liquid ammonia, nitric acid and methanol were all laboratory grades. MAS II-Plus microwave of 2.45 GHz from Sineo was used as throughout the process. Fixed conditions of 80 ℃, 18 min and 300 MHz were applied during the process. During the process, $FeCl_2$ and $FeCl_3$ (mol ratio 1:3) were added into 2M HCl followed by addition of 2.2 M $NH_{3(aq)}$ and deionized water. The unreacted reactants were separated using magnet before addition of HNO_3 and $Fe(NO_3)_3$ at 1:1 (v/v). Samples were washed three times using methanol and separated using magnet before drying overnight in a vacuum oven at 80 ^oC for characterization and enzyme immobilization.

2.2 Characterization on Maghemite Nanoparticle

Morphology of synthesized maghemite was captured using field emission scanning microscopy (Zeiss Supra 35 VP). Degree of magnetization was visualized using Vibrating Sample Magnetometer (VSM) model Lakeshore7404 series in a magnetic field up to ±12 kOe at room temperature. Thermal properties of synthesized maghemite were investigated through differential scanning calorimetry (DSC) under a nitrogen flow with rate of 50 ml min^{-1}.

2.3 Immobilization of Lipase on Maghemite

Maghemite was treated with chitosan before undergoes immobilization process. 1% (w/w) chitosan was dissolved in 1.5% (v/v) acetic acid of pH 4.0. Then, 0.1 g of maghemite was added into 20 ml of prepared chitosan. The excess chitosan was removed by washing the solution with deionized water and separated with external magnet. The complex was then dispersed into 0.5 mg/ml sodium tripolyphosphate (TPP) to form maghemite/chitosan/TPP composite. Immobilization of lipase was conducted in a thermal shaker incubator at 200 rpm, 9 hrs incubation time and 55 ℃ incubation temperature. The immobilized lipase was separated by applying external magnet post treatment. Enzyme activity was calculated through hydrolysis of *p*- nitrophenyl palmitate at 37 ℃. The released *p*-nitrophenol was quantified using UV-Vis spectrophotometer at 410 nm. The unit used to determine the enzyme activity is noted as U; where it explains the amount of immobilized lipase enzyme required to hydrolyze 1 µmol of *p*-nitrophenyl palmitate per minute.

3. RESULTS AND DISCUSSIONS

3.1 Production of Maghemite and Its Characterization

Produced maghemite was separated from reaction mixture by applying external Calamit magnetic iron remover. The recovered maghemite was then subjected for vacuum drying overnight to remove excess solvent. Dry weight of recovered maghemite was recorded at 0.362 g. Distribution pattern for synthesized maghemite was evaluated through FESEM. Based on the microscopic image (Figure 1), the magnetic nanoparticles were seen to be homogenously in spherical shape with average size distribution of ~20 nm.

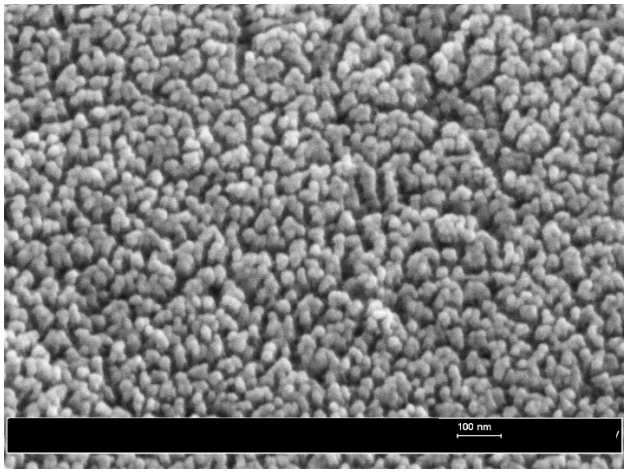

Figure 1. Snapshot of FESEM on the maghemite nanoparticles

Magnetic behavior of maghemite was evaluated using vibrating sample magnetometer (VSM) at room temperature. Based on Figure 3, the saturation magnetization (M_s) of synthesized maghemite was recorded at 60.1 emu/g which is in approximation to the bulk maghemite (60 emu/g) thus explaining the high purity of synthesized products (Guivar, Martínez and Anaya, 2014; Kamel Ariffin, Idris and Ngadiman, 2018). The pattern of hysteresis loop is highly dependent on the size of nanoparticles. Small size of maghemite nanoparticles resulted in superparamagnetic properties with negligible coercivity value (H_c). ~4 Oe was recorded for the coercivity value. The magnetic behaviour of synthesized maghemite is shown in Figure 2.

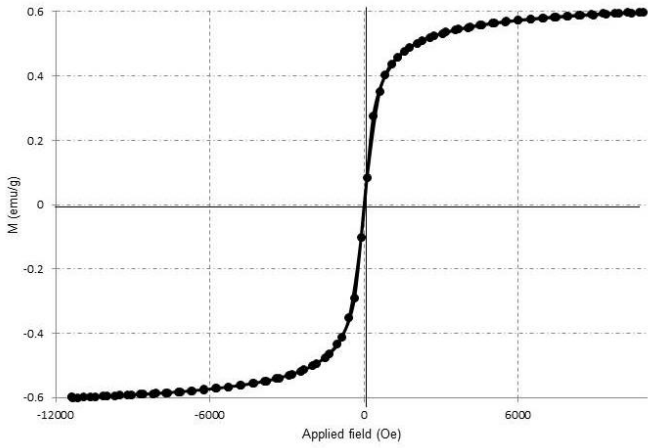

Figure 2. Hysteresis curve of synthesized ferrofluid at 300 K.

The thermogram of synthesized maghemite was recorded using Dielectroscanning Calorimetry (DSC). The thermogram proceeds from room temperature up to 480 ℃. An exothermic peak was evident at 456 ℃ indicating the nanomaterial phase change towards becoming hematite (Rocher *et al.,* 2013). The enthalpy of transition was recorded at 140.55 J/g. The entropy in the system was also calculated using transition temperature (℃) and enthalpy (J g^{-1}) values and the value obtained was 0.31 J g^{-1} $℃^{-1}$.

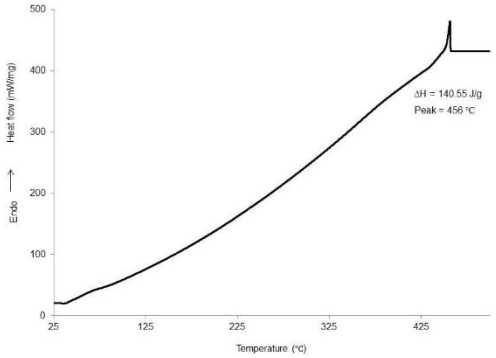

Figure 3. DSC curve for synthesized maghemite.

3.2 Lipase Immobilization on Synthesized Maghemite

Synthesized maghemite was subjected for surface modification to assist amine group linkage from the enzyme group to the maghemite nanoparticles. Maghemite/chitosan/TPP composite was synthesized through cross-linking reaction. Immobilization reaction was performed in a thermo-control shaking incubator at optimum condition based on our previous experiment (data not shown). The activity of immobilized lipase was measured using UV –Vis spectrophotometer at 410 nm based on hydrolysis of *p*-nitrophenyl palmitate ester in a buffered oil/water emulsion at 37 ℃ was recorded at 1.8 U.

4. CONCLUSION

Maghemite nanoparticles were successfully synthesized *via* microwave assisted technique. The synthesized maghemite possessed superparamagnetic properties that provide wide advantages upon utilization. Upon its manipulation as an enzyme carrier, the maghemite required surface modification to ensure successful immobilization process.

5. ACKNOWLEDGEMENT

The authors acknowledge the financial assistance by HICOE grant (Vote no: 4J268).

REFERENCES

Chiou, S. and Wu, W. (2004) 'Immobilization of Candida rugosa lipase on chitosan with activation of the hydroxyl groups', *Elsevier*.

Guivar, J., Martínez, A. and Anaya, A. (2014) 'Structural and magnetic properties of monophasic maghemite (γ-Fe 2 O 3) nanocrystalline powder', *Advances in*.

Hu, L. *et al.* (2011) 'Microwave-assisted one-step hydrothermal synthesis of pure iron oxide nanoparticles: magnetite, maghemite and hematite', *Journal of Sol-Gel Science and Technology*. Springer US, 60(2), pp. 198–205. doi: 10.1007/s10971-011-2579-4.

Kamel Ariffin, M. F., Idris, A. and Ngadiman, N. H. A. (2018) 'Optimization of One-Pot Microwave-Assisted Ferrofluid Nanoparticles Synthesis Using Response Surface Methodology', *IEEE Transactions on Magnetics*, 54(6), pp. 1–6. doi: 10.1109/TMAG.2018.2816589.

Kim, B. C. *et al.* (2005) 'Preparation of biocatalytic nanofibres with high activity and stability via enzyme aggregate coating on polymer nanofibres', *Nanotechnology*, 16(7), pp. S382–S388. doi: 10.1088/0957-4484/16/7/011.

Osborne, E. A. *et al.* (2012) 'Rapid microwave-assisted synthesis of dextran-coated iron oxide nanoparticles for magnetic resonance imaging', *Nanotechnology*. IOP Publishing, 23(21), p. 215602. doi: 10.1088/0957-4484/23/21/215602.

Rocher, V. *et al.* (2013) 'Direct amine-functionalisation of γ-Fe 2 O 3 nanoparticles'. doi: 10.1039/c3dt52386a.

Romdhane, I., Romdhane, Z. and Gargouri, A. (2011) 'Esterification activity and stability of Talaromyces thermophilus lipase immobilized onto chitosan', *Elsevier*.

EFFECT OF MOMORDICA CHARANTIA TREATMENT ON INFLAMMATORY RESPONSES IN RAW264.7 CELLS

Shi Yan Lee[1], Won Fen Wong[2] and Kian-Kai Cheng[3]
[1]*Innovation Centre in Agritechnology for Advanced Bioprocessing (ICA), Universiti Teknologi Malaysia, 84600 Pagoh, Johor.*
leeshiyan0520@gmail.com

[2]*Department of Medical Microbiology, Faculty of Medicine, University of Malaya, 50603 Kuala Lumpur.*
wonfen@um.edu.my

[3]*Innovation Centre in Agritechnology for Advanced Bioprocessing (ICA), Universiti Teknologi Malaysia, 84600 Pagoh, Johor.*
chengkiankai@utm.my

ABSTRACT

Momordica charantia, also known as bitter gourd, is a fruit that is widely cultivated and available in Asia, India, East Africa, and South America. It is consumed as food or folk medicine in many Asian countries. *Momordica charantia* is known for its anti-diabetic, anti-inflammatory, anti-oxidant, anti-cancer, anti-microbial activities. However, the detailed molecular mechanism of its anti-inflammatory action is yet to be elucidated. This project aimed to examine the effects of *Momordica charantia* on modulating LPS-induced inflammation in RAW 264.7 macrophages. MTT tests were used to determine the cytotoxicity of *Momordica charantia* freeze-dried powder in RAW264.7 cells and real-time PCR was applied to analyze the expression of inflammatory genes in the RAW264.7 cells treated with lipopolysaccharide (LPS) with or without *Momordica charantia* powder. The study also looked into the effect of *Momordica charantia* treatment on inflammatory protein markers expression of LPS-induced RAW264.7 cells such as NF-kB, IKKB and IKB-alpha using Western-Blot analysis. Notably, the current results showed that *Momordica charantia* treatment led to marked reduction in inflammatory responses. Our study provided evidences supporting high anti-inflammatory activities of *Momordica charantia*.

Keywords: Bitter gourd; anti-inflammation; gene expression; protein expression

1. INTRODUCTION

Inflammation is a response of host responding to harmful stimuli. There are two main types of inflammation which are acute inflammation and chronic inflammation. Acute inflammation is refered as biological protective mechanism of organism towards an injury, irritation or surgery [1]. It is characterized by redness, swelling and pain. If acute inflammation is left untreated, it will lead to chronic inflammation. Chronic inflammation is associated with various chronic diseases including cancer, cardiovascular diseases, Alzheimer's disease, type II diabetes mellitus, arthritis, auto-immune diseases, neurological diseases and pulmonary diseases [2,3].

Lipopolysaccharide (LPS) is a prototypical endotoxin found in the outer membrane of Gram-negative bacteria. It is a potent innate immune-activating stimuli which can directly activate macrophages [4]. Mouse macrophages, RAW264.7 is an efficient model for investigating infection-related pro-inflammatory responses. It can be activated by LPS leading to the production of measurable inflammatory mediators such as leukotrienes, TNF-α and interleukins (ILs) [5].

Momordica charantia (MC) is also known as bitter melon, bitter gourd and karela. It is widely cultivated and used as food in Asia, Africa and South America. It is known for its therapeutic roles in traditional medicine. Extracts of MC were reported to possess anti-oxidant, anti-diabetic, anti-cancer, anti-inflammatory, anti-bacterial, antifungal, anti-viral, anti-HIV, anti-helminthic, anti-mycobacterial, hypotensive, anti-obesity, immunomodulatory, anti-hyperlipidemic, hepatoprotective and neuroprotective activities [6]. MC can suppress lipopolysaccharide-stimulated inflammatory responses in macrophages through the inhibition of NF-κB activation [7]. The ethanol extract of bitter gourd reduced LPS-induced nitric oxide, inducible nitric oxide synthase (iNOS), prostaglandin E2 (PGE2) and pro-interleukin-1 beta expression [7]. In mouse model, administration of freeze-dried MC

powder also significantly decreases the protein levels of NF-κB, JNK and cyclooxygenase-2 (COX2), and inducible nitric oxide synthase [8].

The biological activities of MC show potential pharmacological value. Understanding the mechanism of the anti-inflammatory activities of MC could therefore provide therapeutic clues to modulate inflammatory disease using a plant or herb based dietary supplementation.

2. MATERIALS AND METHODS

2.1 Cell Culture

RAW264.7 were purchased from ATCC (TIB71). RAW264.7 were cultured in DMEM (Gibco, Thermo Fisher Scientific) supplemented with 10% fetal bovine serum, penicillin G (100 mg/ml), and streptomycin (100 mg/ml). Cells were maintained at 37°C in 5% CO_2 in a humidified incubator.

2.2 MC Sample Preparation

MC sourced from local distributor located in Johor, Malaysia was cleaned and the seeds were removed. The fruits were cut into 2mm thin pieces and kept in -20°C freezer. After that, the frozen fruits were freeze dried using Cuddon FD80 freeze dryer and milled into fined powder. The MC powder were then reconstituted with MiliQ water in 1: 9 ratio and filtered with 0.2 μm syringe filter followed by 3kDa spin column before the cell culture experiment.

2.2 Cell Proliferation Assay

A total number of 1.0 x 10^4 cells per well were seeded into a 96- well plate and incubated overnight at 37°C in 5% CO_2. The next day, the cells were treated with a two-fold serial dilution of MC powder. MTT assays were performed [9]. After 24 h, (4,5-dimethylthiazol-2-yl-2,5-diphenyltetrazoliumbromide) was added at 2 mg/ml. After 3 h of incubation at 37°C in 5% CO_2, DMSO was added to dissolve the formazan crystals. The plates were then read in Synergy HTX multi-mode reader (BioTek) at 570 nm absorbance. The ratio of the absorbance of treated cells to the absorbance of DMSO- treated control cells was determined as percentage cell viability. The concentration of compounds which resulted in a 50% reduction in viability was defined as the IC_{50}.

2.3 Inflammatory Gene Expression

Cells in T25 flask with 80% confluency pretreated with or without 12.5% MC powder for 4 hours were incubated with 1μg/ml LPS for 4 hours. Total RNAs were extracted using TRIzol (invitrogen, Thermo Fisher Scientific). Complimentary DNAs were synthesized SuperScript IV kits (invitrogen, Thermo Fisher Scientific) and Real Time PCR was performed with SYBR Green PCR Master mix (Thermo Fisher Scientific) and run on the Agilent Stratagene Mx3000P Real-Time PCR System.

2.4 Inflammatory Protein Markers Expression

Cells in T25 flask with 80% confluency were treated with or without 12.5% MC powder and 1μg/ml LPS for 24 hours. Cell lysate were collected using RIPA Lysis Buffer (Santa Cruz Biotechnology). Protein samples was separated on 10% Tris-Gly gel and transferred to polyvinylidene difluoride membranes. The membranes were then incubated in 5% skimmed milk in TBST buffer to block non-specific binding at room temperature for one hour followed by incubation with primary antibodies (Cell Signaling Technology) overnight at 4°C. After that, the membranes were washed three times in TBST for five minutes each and incubated with secondary antibodies (Promega Corporation) for one hour at room temperature. The membranes were stained and view using HP 4050 membrane scanner.

3. RESULTS AND DISCUSSION

3.1 IC_{50}

The effect of MC powder on cell viability was evaluated by use of the MTT assay. The value of IC_{50} is 30.48%.

3.2 Inflammatory Gene Expression

LPS upregulated the expression of pro-inflammatory genes such as IL6, TNF- α, IL1B, COX2 and iNOS. The treatment of 12.5% MC powder significantly reduce the expression of the pro-inflammatory genes.

4. CONCLUSION

The finding revealed that *Momordica charantia* exerted anti-inflammatory effects by down-regulating IL6, TNF- α, IL1B, COX2 and iNOS gene expression and inhibit activation of NF-κB and IKK-β. These findings provided new insights in understanding the complex biological action of MC in immune response and suggest that it could serve as a potential selective modulator to treat inflammation associated diseases.

ACKNOWLEDEMENTS

Shi Yan Lee is supported by Ainuddin Wahid Scholarship. The work is supported by Malaysia Toray Science Foundation (4B324) and Research University Grant from Universiti Teknologi Malaysia (18H73 and 14H62).

REFERENCES

1. Meixia Huo, Xiurui Cui, Jiangdong Xue, Gefu Chi, Ruijie Gao, Xuming Deng, Shuang Guan, Jingyuan Wei, Lanan Wassy Soromou, Haihua Feng and Dacheng Wang. (2013). Anti-inflammatory effects of linalool in RAW 264.7 macrophages and lipopolysaccharide-induced lung injury model, Journal of Surgical Research, I80, E47-E54.
2. Hummasti, S. and Hotamisligil, G.S. (2010). Endoplasmic reticulum stress and inflammation in obesity and diabetes, Circulation Research, 107, 5, 579-591.
3. Lee IT, Yang CM. (2013). Inflammatory signaling involved in airway and pulmonary diseases, Mediators Inflamm, 791231.
4. Rossol M., H. Heine, U. Meusch, D. Quandt, C. Kleain, M.J. Sweet, and S. Hauschildt. (2011). LPS-induced cytokine production in human monocytes and macrophages, Critical Reviews in Inmmunology, 31, 379-446.
5. Guan-Wei Fan, Yuan Zhang, Xiaorui Jiang, Yan Zhu, Bingyao Wang, Lina Su, Wenjie Cao, Han Zhang and Xiumei Gao. (2013). Anti-inflammatory Activity of Baicalein in LPS-Stimulated RAW264.7 Macrophages via Estrogen Receptor and NF- κB-Dependent Pathways, Inflammation, 36, 6, 1584-91.
6. Prasad R. Dandawate, Dharmalingam Subramaniam, Subhash B. Padhye, and Shrikant Anant. (2016). Bitter melon: a panacea for inflammation and cancer, Chin J Nat Med., 14, 2, 81-100.
7. Lii CK, Chen HW, Yun WT, Liu KL. (2009). Suppressive effects of wild bitter gourd (Momordica charantia Linn. Var. abbreviate ser.) fruit extracts on inflammatory responses in RAW 264.7 macrophages, J Ethnopharmacol, 122, 227-233.
8. Yang SJ, Choi JM, Park SE, Rhee EJ, Lee WY, Oh KW, Park SW, Park CY. (2015). Preventive effects of bitter melon (Momordica charantia) against insulin resistance and diabetes are associated with the inhibition of NF-κB and JNK pathways in high-fat-fed OLETF rats, J Nutr Biochem, 26, 3, 234-40.

9. Looi CY, Imanishi M, Takaki S, Sato M, Chiba N, et al. (2011) Octa-arginine mediated delivery of wild-type Lnk protein inhibits TPO-induced M-MOK megakaryoblastic leukemic cell growth by promoting apoptosis, PLoS One, 6, e23640.

EFFECTS OF COMBINED CISPLATIN AND CLINACANTHUS NUTANS ON GENE EXPRESSION OF MDA-MB-231 BREAST CANCER CELLS

Yeo Zhin Leng[1], Nur Fitriyani Afiqah binti Abu Bakar[1], Priya Madhavan[2], Vuanghao Lim[3] and Praseetha Prabhakaran[1*]

[1]*Universiti Teknologi Malaysia (Department of Biosciences, Faculty of Science, 81310 UTM Skudai, Johor, Malaysia; zhinleng94@gmail.com*

[1]*Universiti Teknologi Malaysia (Department of Biosciences, Faculty of Science, 81310 UTM Skudai, Johor, Malaysia; fitriyaniafiqah@gmail.com)*

[2]*Taylors University (School of Medicine, Taylor's University, No.1 Jalan Taylor's, 47500 Subang Jaya, Selangor, Malaysia; Priya.Madhavan@taylors.edu.my)*

[3]*Integrative Medicine Lab, Advanced Medical and Dental Institute, Universiti Sains Malaysia, Penang, Malaysia*
[1]*Universiti Teknologi Malaysia (Department of Biosciences, Faculty of Science, 81310 UTM Skudai, Johor, Malaysia; praseetha@fbb.utm.my)*

ABSTRACT

Triple Negative Breast Cancer is the most invasive breast cancer subtype enriched with cancer stem cells. Absence of Estrogen, Progesterone and HER2 receptors make TNBCs difficult to be targeted by existing chemotherapy treatments. This study was aimed at identifying the effects of the cisplatin-*C.nutans* combined therapy on the gene expression of MBA-MD-231 cells representing the TNBC subtype. Both cisplatin and *C. nutans* especially as combined treatment exhibited potent anticancer effects on MDA-MB-231 breast cancer cells. Cisplatin at (0.76, 1.52, 3.05, 4.57, 6.10, and 15.23 µg/mL), *C. nutans* at (2.5, 5, 10, 20, 30, and 50 µg/mL) and combination of cisplatin (3.05 µg/ml) with *C. nutans* at (0, 2.5, 5, 10, 20, 30, and 50 µg/ml) were tested on MDA-MB-231 for cell viability. Cisplatin and *C. nutans* reduced cell viability in a dose-dependent manner by 7.05-57.47% (cisplatin), 7.02-50.29% (*C. nutans*) and 8.36-75.79% (combined cisplatin-*C. nutans*). Single cisplatin and *C. nutans* treatment respectively induced differentiation while the combined treatment induced apoptosis in MDA-MB-231 cells. Furthermore, cisplatin and *C. nutans* differentially regulated specific genes in which differentiation markers KRT18 and ß–tubulin (solo cisplatin and *C. nutans* treatment) and KLF4 (all treatments) were up-regulated while CD49f (cisplatin and combination treatment) was down-regulated. These findings altogether suggest that the cisplatin-*C.nutans* combination is a potent anticancer agent for the targeted therapy of MDA-MB-231 cells and other CSC-enriched cancers. The up-regulation of KLF4 correlating to increased differentiation of CSCs can be highlighted as an important cancer prognostic marker for the treatment and management of TNBC.

Keywords: Triple Negative Breast Cancer, Cisplatin, *Clinacanthus nutans*, Proliferation, Differentiation

1. INTRODUCTION

Cancer is a dangerous disease and was ranked as the second highest affected disease that lead to death of earth's population after heart disease in 2013 (Fitzmaurice *et al.*, 2015). Breast cancer is an uncommon group of disease consisting of tumour cells ranging from stem cell-like to more differentiated cells (Prabhakaran *et al.*, 2013). The triple negative breast cancer (TNBC) subtype lacks three important hormone receptors mainly the estrogen receptor (ER) and progesterone receptor (PR) and also human epidermal growth factor receptor 2 (HER2) (Dai *et al.*, 2015; Denkert *et al.*, 2017). TNBCs are known to be enriched with functional cancer stem-like cells, exhibit high migration pattern and express some specific breast cancer genes making them as the most invasive subtype among breast cancers. In recent years, the TNBCs have however shown specific sensitivity towards cisplatin, the first metal based anti-cancer drug (Prabhakaran *et al.*, 2013; Al-Bahlani *et al.*, 2017b). Cisplatin is a well-known cytotoxic drug that is claimed to be capable of interfering with the DNA activity upon entering the nucleus of the cells and preventing the DNA repair process. This

event eventually leads to cell death (Al-Bahlani *et al.*, 2017a). Nevertheless, some recent studies have shown that cisplatin may possess other mechanism of action such as inducing differentiation of cancer cells apart from apoptosis (Prabhakaran *et al.*, 2013). Although previous studies pointed out that cisplatin give rise to some side effects after initial treatment (Cepeda *et al.*, 2007) however, accumulated evidence showed that co-treatment of cisplatin with other potential anticancer drugs induces apoptosis or autophagy in various cancer cells (Al-Bahlani *et al.*, 2017b;Yu *et al.*, 2017). In contrast, *Clinacanthus nutans* (*C. nutans*) is a traditional herb that is claimed to be a potential chemoprevention alternative for cancer patients (Fazil *et al.*, 2016). *C. nutans* extracts contain various types of phytochemical compounds with useful biological capabilities (Ghasemzadeh *et al.*, 2014; Zakaria *et al.*, 2017). Natural-derived phytochemical constituents in *C. nutans* extracts also found to exhibit cytotoxicity effects through the induction of apoptosis and antioxidant activity that could reduce the risk of getting cancers (Ghasemzadeh *et al.*, 2014; Zakaria *et al.*, 2017). In conclusion, this study mainly focuses on determining the anticancer effects of both cisplatin and *C. nutans* as well as combination of these two drugs, on the other hand also examine the effects of the drug treatments affecting the gene regulation on MDA-MB-231 cells.

2. MATERIALS AND METHODS

2.1 Drugs

a. Cisplatin
b. Clinacanthus nutans

2.2 Cell Culture

MDA-MB-231 cells representing the TNBCs was cultured and maintained in T25 flasks at 37^{o}C and 5% CO_2 Dulbecco's Modified Eagle's Medium (DMEM)/F12 + glutamax^{TM} (Gibco by Life Technologies) enriched with 10% fetal calf serum (FBS) and 1% antibiotic-antimycotic (100 U/mL penicillin, 100 µg streptomycin/0.25 µg/mL). Cells were passaged approximately 3 times per week.

2.3 Viability Assay

The Cell Titer-Glo® 2.0 Assay kit (Promega, United States) was used to examine the cell viability of MDA-MB-231 cells. Approximately 4000 cells/100 µL per well were seeded in a 96-well plates. After 24 hours of incubation, different concentrations of cisplatin (0.76, 1.52, 3.05, 4.51, 6.10, and 15.23 µg/mL) and *C. nutans* (0, 2.5, 5, 10, 20, 30, and 50 µg/ml) were added to each well respectively and was further incubated for another 24 hours. As for the combination treatment, cells will first be treated with 3.05 µg/mL Cisplatin and incubated for 24 hours followed by treatment with (0, 2.5, 5, 10, 20, 30, and 50 µg/ml) *C. nutans* and incubated further for 24 hours. Next, frozen Cell Titer-Glo® 2.0 Reagent was thawn and equilibrated to room temperature for 30 minutes prior to use. Next, each well was added with 100 µL of the Cell Titer-Glo® 2.0 Reagent (ratio 1:1), 2 minute of slow mixing to lyse the cells followed by another 10 minutes of incubation. Lastly, the luminescence activity of the cells was measured by using GloMax®-Multi Detection System (Promega, United States).

2.4 Apoptosis Assay

The Caspase-Glo® 3/7 Assay kit (Promega, United States) was used to examine the ability of the drugs to induce apoptosis in MDA-MB-231 cells. Approximately 4000 cells/100 µL per well were seeded in a 96-well plates. After 24 hours of incubation, the cells were treated with the IC_{50} concentrations (4.51 µg/mL cisplatin, 50 µg/mL *C. nutans* and combination: 3.05 µg/mL cisplatin and 10 µg/mL *C. nutans*) respectively. Cells were also treated with 20 nM of Taxol, a positive control drug. Caspase-Glo® 3/7 Reagent was added carefully with the ratio of 1:1 which is 100 µL into each well to avoid cross-contamination. The plate was be covered with aluminium foil and swirled slowly for 30 seconds to ensure homogenization. The following incubation process was done at room temperature for 1 hour. Finally, the luminescence measurements were taken by using GloMax®-Multi Detection System (Promega, United States).

2.5 QRT Polymerase Chain Reaction (PCR)

The cDNA products were prepared at 20 ng/µL per sample respectively. 1 µL of cDNA were mixed with 10 µL of 2x SsoAdvanced™ universal SYBR® Green supermix (Bio-rad, United States) and 9 µL of nuclease-free water in a skirted 96-well PCR plate with specific targeted genes inside to detect the relative abundance of the gene expression before and after the different treatments. Universal SYBR® Green supermix was used in qRT-PCR to assist in the fluorescent signalling in gene expression levels. In addition, 1 µL of PCR control assay template was added into the positive control well. PCR control assay template lyophilized in the bottle was prepared by adding 200 µL of TE buffer. The master mix prepared were mixed thoroughly and distributed equally into the wells of PCR plate and sealed with transparent film. The PCR mixtures were then incubated at Bio-rad iCycler TM Optical Module (Bio-rad, United States) with the reaction protocol of 95°C for 2 minutes (1 cycle for activation step), 95°C for 5 seconds (40 cycles for denaturation step), 60°C for 30 seconds (40 cycles for annealing/extension step), and 65-95°C for 5 seconds (1 step for melt curve). Positive controls used include PCR control assay template, RQ1 and RQ2 (RNA integrity checking), and RT (reverse transcriptase checking) while negative control includes gDNA (genomic DNA contamination checking).

2.6 Statistical Analysis

Statistical analysis of the results was done in Microsoft Excel and GraphPad Prism 7. Numerical results obtained were displayed in bar graphs and dose-response curve to compare the controls and cell line treated with cisplatin, *C. nutans*, and combined cisplatin-*C. nutans*. Another sets of numerical results obtained were also illustrated in bar graphs to compare and observe the differences in gene expression of specific markers with the housekeeping genes. The outcome of the results were showed as mean±standard error mean (SEM) for cell viability assay, apoptosis assay, and also qRT-PCR.

3. RESULTS AND DISCUSSION

3.1 Cisplatin and *C. nutans* Reduced Cell Viability of MDA-MB-231 Cells

Both solo Cisplatin and *C.nutans* treatments as well as combined Cisplatin-*C.nutans* treatment reduced cell viability in a dose-response manner in MD-MB-231 cells. Cells treated with solo cisplatin and *C. nutans* showed prominent changes of cell morphology in which cells appeared smaller, shrunken and elongated compared to the untreated cells. In contrast, cells treated with the combined cisplatin-*C.nutans* resulted in rounded cells and formation of apoptotic bodies along with the shrunken and elongated cells with increasing *C. nutans* concentration. A fixed 3.05 µg/mL cisplatin treatment for 24 hours prior to various (10-50 µg/mL) *C. nutans* treatment for a further 24 hours revealed that C. nutans sensitized MDA-MB-231 cells to cisplatin treatment by significantly increasing the cell growth inhibition compared to mono 3.05 µg/mL cisplatin (23.58%) and mono 10-50 µg/mL *C. nutans* (20.64%, 37.75%, 40.5%, and 57.47% respectively to (53.08%, 59.88%, 67.05%, and 75.79%) in the combined (3.05 µg/mL cisplatin + 10-50 µg/mL C. nutans). In addition to that, the new IC_{50} concentration achieved upon the combined treatment is 7.53 µg/mL compared to mono cisplatin (11.73 µg/mL) and mono *C. nutans* (49.37 µg/mL). Therefore, it can be concluded that combination of cisplatin and *C. nutans* in a treatment showed better cytotoxicity effect in which cisplatin sensitized MDA-MB-231 cells towards *C. nutans* treatment. Moreover, the combined treatment also required much lower cisplatin as well as *C. nutans* doses which was sufficient to exert a more significant inhibitory effect on MDA-MB-231.

3.2 Mono Cisplatin and C.nutans Induced Differentiation while Combined Cisplatin-C.nutans induced apoptosis in MDA-MB-231 Cells

20 nM Taxol and combined (3.05 µg/mL cisplatin + 10 µg/mL *C. nutans*) clearly induced significant apoptosis (0.14% and 1.76%) respectively as compared to control. In contrast, 11.73 µg/mL cisplatin and 49.37 µg/mL *C. nutans* treated MDA-MB-231 cells showed an insignificant or negligible increase (0.04% and 0.01%) of caspase activity which indicates inability of both solo cisplatin and *C. nutans* to induce apoptosis.

3.3 Differential Gene Regulation of KLF4, KRT18, TUBA1A and CD49f in Cisplatin and *C. nutans*-treated MDA-MB-231 Breast Cancer Cells

All these genes studied were expressed by MDA-MB-231 cells and the expressions were affected upon treatment with solo cisplatin, mono *C. nutans* and combined cisplatin-*C. nutans*. An obvious and significant upregulation of KLF4, RNA expression was observed in MDA-MB-231 cells upon all treatments (cisplatin, 6.256; *C. nutans*, 10.214; combination, 8.436) respectively as compared to the expression of other genes. Similarly, RNA expression of both KRT18 and TUBA1A were also up-regulated upon solo cisplatin and C. nutans treatment, however a down-regulation was observed in KRT18 expression (39%) and up-regulation in TUBA1A expression (19%) upon combined cisplatin-*C. nutans* treatment. In contrast to the increased RNA expression pattern of KLF4, CD49f expression was down-regulated upon cisplatin (19%) and combined cisplatin-*C. nutans* (22%) treatment. KLF4 is a transcription factor that is highly expressed in most of the breast cancer cells (Yu *et al.*, 2011). KLF4 acts as transcriptional factor responsible for epithelial cell proliferation and differentiation (Yori *et. al*., 2010). Recent studies showed that high KLF4 expression in TNBC patients correlated with a better overall survival and disease-free survival rates (Nagata *et al.*, 2017) as well as correlated with sensitisation of cancer cells to cisplatin and paclitaxel treatment (Park *et al.*, 2017). In addition to that, (Zhang *et al.*, 2010) have shown that KLF4 interact with Nanog, another TF to prevent ESC differentiation, however the knockdown of Nanog resulted in the differentiation. This argument can be well correlated with MDA-MB-231 cells as these invasive TNBC cells are enriched with CSCs however lack Nanog gene expression (Ling *et al.*, 2012). Therefore, the lack of Nanog expression by MDA-MB-231 cells may have switched the role of KLF4 to the tumour suppressor mode which consequently induced differentiation upon cisplatin and *C. nutans* treatment. In contrast the combined treatment resulted in a rapid decrease of MDA-MB-231 cell viability by almost 30% compared to mono cisplatin and *C. nutans* treatment respectively. The enhanced cell death is mainly induced by apoptosis as exhibited apoptotic body formation and by the increased caspase-3/7 activity. This finding may suggest that 24 hours cisplatin incubation (although at a much lower dose) prior to *C. nutans* treatment induced differentiation of the MDA-MB-231 CSCs which then upon *C. nutans* treatment underwent apoptosis. It is known that more differentiated tumour cells are more sensitive to chemotherapeutic drugs. As such, it can be presumed that *C. nutans* in fact may possess a dual mechanism in which it can chose either to induce differentiation or apoptosis depending on the cancer cell phenotype via activation of different cancer pathways.

4. CONCLUSION

As a whole, these findings altogether suggest that both cisplatin and *C. nutans* are potent anticancer targets especially in combination for the targeted therapy of TNBCs as portrayed by the MDA-MB-231 cells and possibly for other cancers enriched with CSCs. Lastly, the high level up-regulation of KLF4 correlating to increased differentiation of CSCs can be highlighted as an important cancer prognostic marker for the treatment and management of TNBC. Further studies are required to gain deeper understanding regarding the involved mechanism carried out by cisplatin and *C. nutans*. Future research should also be carried out to determine whether epigenetic regulation is involved at a post-translational level upon mono and/or combined cisplatin and *C. nutans* treatments which can be examined via immunofluorescence microscopy and flow cytometry. Lastly, effects of cisplatin and *C. nutans* toxicity level could be carried out on normal mammary cells in order to select a suitable drugs dosage that exerts anticancer effects for better therapeutic treatment with lesser side effects.

ACKNOWLEDGEMENT

The authors are thankful to Ministry of Education (MOHE) for contributing to this research findings by providing the Fundamental Research Grant Scheme (FRGS)(Cost Center: R.J130000.7845.4F769) to fund this study.

REFERENCES

1. Al-Bahlani, S., Al-Lawati, H., Al-Adawi, M., Al-Abri, N., Al-Dhahli, B., and Al-Adawi, K. (2017a). Fatty acid synthase regulates the chemosensitivity of breast cancer cells to cisplatin-induced apoptosis. *Apoptosis, 22*(6), 865-876.
2. Al-Bahlani, S. M., Al-Bulushi, K. H., Al-Alawi, Z. M., Al-Abri, N. Y., Al-Hadidi, Z. R., and Al-Rawahi, S. S. (2017b). Cisplatin induces apoptosis through the endoplasmic reticulum-mediated, calpain 1 pathway in triple-negative breast cancer cells. *Clinical breast cancer, 17*(3), e103-e112.
3. Cepeda, V., Fuertes, M. A., Castilla, J., Alonso, C., Quevedo, C., and Pérez, J. M. (2007). Biochemical mechanisms of cisplatin cytotoxicity. *Anti-Cancer Agents in Medicinal Chemistry (Formerly Current Medicinal Chemistry-Anti-Cancer Agents), 7*(1), 3-18.
4. Dai, X., Li, T., Bai, Z., Yang, Y., Liu, X., Zhan, J., et al. (2015). Breast cancer intrinsic subtyp classification, clinical use and future trends. *American journal of cancer research, 5*(10), 2929.
5. Denkert, C., Liedtke, C., Tutt, A., and von Minckwitz, G. (2017). Molecular alterations in triple-negative breast cancer—the road to new treatment strategies. *The Lancet, 389*(10087), 2430-2442.
6. Fazil, F. N. M., Azzimi, N. S. M., Yahaya, B. H., Kamalaldin, N. A., and Zubairi, S. I. (2016). Kinetics Extraction Modelling and Antiproliferative Activity of Clinacanthus nutans Water Extract. *The Scientific World Journal, 2016*.
7. Fitzmaurice, C., Dicker, D., Pain, A., Hamavid, H., Moradi-Lakeh, M., MacIntyre, M. F., et al. (2015). The global burden of cancer 2013. *JAMA oncology, 1*(4), 505-527.
8. Ghasemzadeh, A., Nasiri, A., Jaafar, H. Z., Baghdadi, A., and Ahmad, I. (2014). Changes in phytochemical synthesis, chalcone synthase activity and pharmaceutical qualities of Sabah snake grass (Clinacanthus nutans L.) in relation to plant age. *Molecules, 19*(11), 17632-17648.
9. Ling, G.-Q., Chen, D.-B., Wang, B.-Q., and Zhang, L.-S. (2012). Expression of the pluripotency markers Oct3/4, Nanog and Sox2 in human breast cancer cell lines. *Oncology letters, 4*(6), 1264-1268.
10. Nagata, T., Shimada, Y., Sekine, S., Moriyama, M., Hashimoto, I., Matsui, K., et al. (2017). KLF4 and NANOG are prognostic biomarkers for triple-negative breast cancer. *Breast cancer, 24*(2), 326-335.
11. Park, Y.-K., Wang, L., Giampietro, A., Lai, B., Lee, J.-E., and Ge, K. (2017). Distinct roles of transcription factors KLF4, Krox20, and peroxisome proliferator-activated receptor γ in adipogenesis. *Molecular and cellular biology, 37*(2), e00554-00516.
12. Prabhakaran, P., Hassiotou, F., Blancafort, P., and Filgueira, L. (2013). Cisplatin induces differentiation of breast cancer cells. *Frontiers in oncology, 3*.
13. Yu, F., Li, J., Chen, H., Fu, J., Ray, S., Huang, S., et al. (2011). Kruppel-like factor 4 (KLF4) is required for maintenance of breast cancer stem cells and for cell migration and invasion. *Oncogene, 30*(18), 2161.
14. Zakaria, K. N., Amid, A., and Jamal, P. (2017). A Review of Anticancer, Antitumor, and Antioxidant of Clinacanthus nutans. *AsPac J. Mol. Biol. Biotechnol., 25*(1).
15. Zhang, P., Andrianakos, R., Yang, Y., Liu, C., and Lu, W. (2010). Kruppel-like factor 4 (Klf4) prevents embryonic stem (ES) cell differentiation by regulating Nanog gene expression. *Journal of Biological Chemistry, 285*(12), 9180-9189.

THE ISOLATION OF PHYTOSTEROLS FROM ORANGE JUICE USING ULTRAFILTRATION

Nurul Hainiza Abd-Razak[1], Y.M. John Chew[2], Michael R. Bird[3*]

[1]*Department of Chemical Engineering, University of Bath, Bath BA2 7AY, UK and Malaysian Rubber Board, 50450 Kuala Lumpur, Malaysia (N.H.B.Abd.Razak@bath.ac.uk)*

[2]*Department of Chemical Engineering, University of Bath, Bath BA2 7AY, United Kingdom (Y.M.Chew@bath.ac.uk)*

[3]*Department of Chemical Engineering, University of Bath, Bath BA2 7AY, United Kingdom (M.R.Bird@bath.ac.uk)*

ABSTRACT

This study describes the use of ultrafiltration membranes to isolate phytosterols from orange juice. A desirable membrane separation rejects proteins whilst transmitting phytosterols and other low molecular weight compounds such as sugars, leading to a concentration of sterols in the permeate. Flat sheet regenerated cellulose membranes with molecular weight cut-off (MWCO) values of 10, 30 and 100 kDa were used. Orange juice was selected as a model solution, being a proxy for natural rubber serum, due to their similarity in the profile of phytosterols compounds in both liquors. The effects of three different membranes upon the rejection of total phytosterols content and antioxidant activity of orange juice were studied. Total phytosterols analysis was carried out by using a Liebermann-Buchard based method. Membranes with MWCO 10 kDa displayed the highest concentration of total phytosterols (40 ± 3 mg/L) in the permeate and a good separation efficiency (32 ± 8% rejection towards phytosterols) from orange juice. Membranes with MWCO 30 kDa and 100 kDa gave higher rejection ratios of total phytosterols; 74 ± 6% and 58 ± 4% respectively, which is both a counter intuitive result, and a less desirable filtration outcome. It is possible that membranes with bigger pores are trapping more protein-based foulants or other hydrophilic submicelles than the small MWCO membrane, leading to an increased rejection of the smaller phytosterol molecules. The overall results showed ultrafiltration could form the basis of a technically feasible solution for isolating phytosterols from orange juice, but subject to further development and process optimisation.

Keywords: Phytosterols; Orange juice; Ultrafiltration; Fouling

1. INTRODUCTION

Plant sterols, generally known as phytosterols, are widely used as food additives due to their ability to lower cholesterol levels in human [1]. Phytosterols are also known for their anticancer properties by inhibiting the progression of cancer cell cycle [2]. Natural rubber serum (NRS) is a by-product of rubber processing and it consists of 1 – 5 wt% non-rubbers such as phytosterols, tocotrienols, lipids, carotenoid, proteins and carbohydrates [3]. It could potentially be exploited for the production of bioactive compounds such as phytosterols. NRS is difficult to obtain in sufficient quantities in a suitable form for experimentation. Thus, orange juice was selected as a model solution, as the amount of phytosterol present is similar to those that in NRS [4]. Membrane technologies such as ultrafiltration (UF) represent an efficient system for the isolation of bioactive compounds from agro-industrial by-products [5]. This paper describes the isolation of phytosterols from orange juice via an ultrafiltration process. The performance of the separation is evaluated in terms of flux, rejection and compound concentration.

2. MATERIALS AND METHODS

2.1 Materials

Orange juice Not From Concentrate was sourced from *Cobell*, UK. The juice was pre-filtered by using a 25 μm cartridge filter (*Memtech*, UK) to remove pulp prior to ultrafiltration. All solvents and

reagents were purchased from *Merck*, UK. Stigmasterol and butylated hydroxytoluene (BHT) acquired from *Sigma Aldrich*, UK were used as characterisation standard. Protein assay kit was acquired from *Bio-Rad*, UK. Three flat-sheet regenerated cellulose (RC) membranes with 10 kDa, 30 kDa and 100 kDa MWCO were supplied by *Alfa Laval*, Denmark.

2.2 Ultrafiltration experimental setup

The ultrafiltration experiments were carried out by using a cross flow membrane filtration system *LabStak M10* manufactured by *DSS* (now *Alfa Laval*), Denmark (Figure 1). The total filtration area of the membrane is 0.036 m^2. The cross flow velocity (CFV) was measured by a rotameter. The pressures were recorded by transducers to calculate the transmembrane pressure (TMP). The ultrafiltration method consists of membrane conditioning, pure water flux (PWF), filtration, rinsing and cleaning steps. These steps have been described in detail by Argyle *et al.* [6].

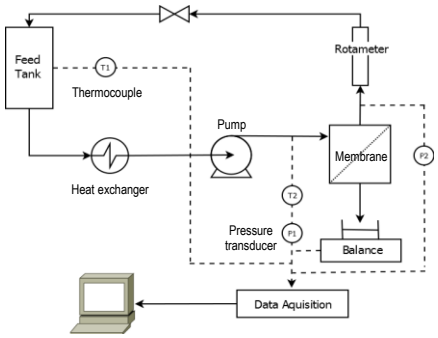

Figure 1. A schematic diagram of the M10 filtration system

2.3 Analyses of phytosterols, proteins, sugar and antioxidant activity

The analysis of phytosterols was performed by using a Liebermann-Buchard (LB) based method [7]. Protein concentration was determined by the Bradford method. The sugar content expressed in °Brix was determined using a refractometer. The antioxidant activity was measured by detecting the scavenging of 1, 1-diphenyl-2-picrylhydrazyl (DPPH) radical.

2.4 Evaluation of permeate flux and selectivity

The effectiveness of membrane process is commonly described in terms of permeate flux and the selectivity [8]. The permeate flux through a membrane can be calculated by:

$$J = \frac{\Delta P}{\mu R} \quad (1)$$

where J is the flux through the membrane (m s^{-1}), ΔP (Pa) is the transmembrane pressure (TMP), μ is the viscosity (Pa s) and R represents the total resistance (m^{-1}). Selectivity is expressed as the rejection ratio (R) and calculated by:

$$R = (1-\frac{C_p}{C_f}) \times 100 \quad (2)$$

where C_p is the solute concentration in the permeate and C_f is the solute concentration in the feed.

3. RESULTS AND DISCUSSION

3.1. Evaluation of Phytosterols, Proteins and Antioxidant Activity

Samples from the feed, retentate and permeate streams were collected and characterised for total phytosterols content, protein, sugar and antioxidant activity. Figure 2 shows the concentration of total phytosterols and protein in feed, retentate and permeate. Total phytosterols originally present in the feed were 0.26 ± 0.01 mg/ml. The highest phytosterols content was achieved in the permeate for 10 kDa membrane (0.15 ± 0.04 mg/ml). Proteins originally present in the feed were 0.87 ± 0.09 mg/ml. Protein concentration was increased in the retentate probably due to the fouling effect.

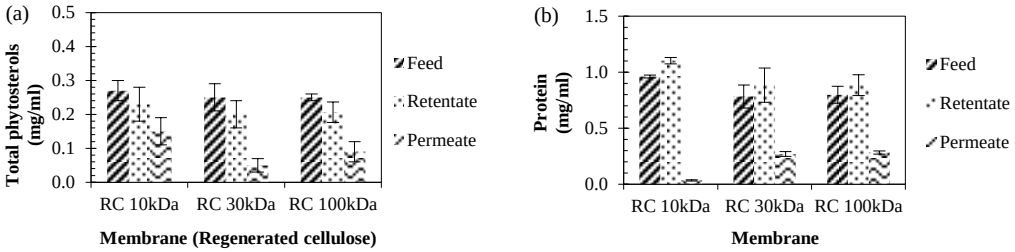

Figure 2. Concentration of (a) total phytosterols and (b) protein in feed, retentate and permeate

3.2 Rejection of Membranes Towards Analysed Compounds

The separation efficiency and the effect of membrane fouling were studied by measuring the rejection of key compounds such as phytosterols, protein, sugar and antioxidant activity (Figure 3). It was reported in the authors' previous work [9] that the 10 kDa RC membrane displayed good separation efficiency with 32 ± 8% rejection towards phytosterols. 30 kDa and 100 kDa membranes showed higher rejection of phytosterols; 74 ± 6% and 58 ± 4% respectively. It is possible that the membrane surface of 30 kDa and 100kDa trapping more foulant due to larger MWCO. Protein was highly rejected (96 ± 1% rejection) by 10 kDa membrane. The 30 kDa and 100 kDa membranes gave lower rejection of protein of 69 ± 3% and 67 ± 2%, respectively. The molecular weight of proteins in orange juice were 12 kDa to 71 kDa [10]. The higher molecular weight compounds were rejected by smaller pore size membrane and this increased the fouling layer [11]. This may suggest that the membrane was fouled by protein-based compounds. All membranes showed lower rejection towards sugar (4% to 6%). For antioxidant activity, the rejection was in the range 12% to 30% Inhibition. No correlation was observed between antioxidant activity and phytosterol content. It is possible that the antioxidant activity detected can be attributed to other chemical compounds present in orange juice, such as phenolic compounds [12].

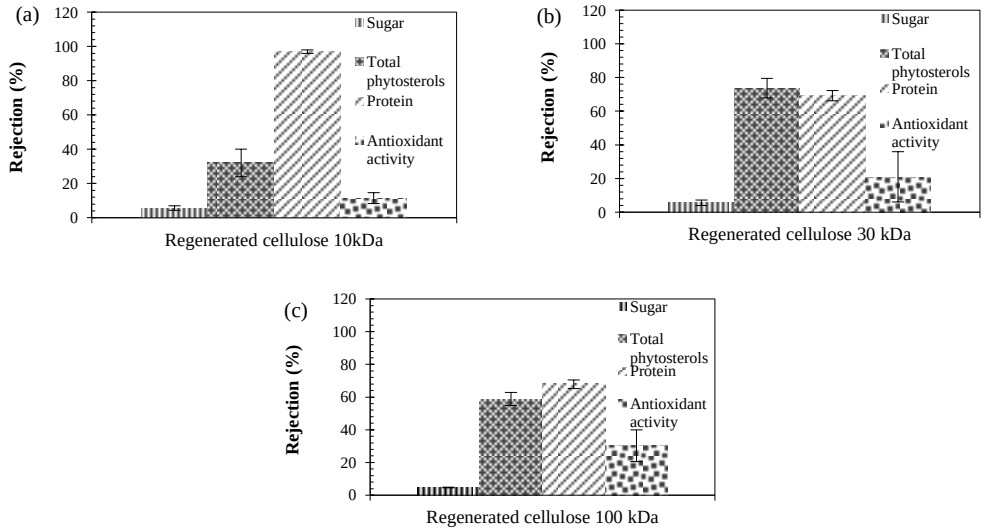

Figure 3. Rejection of compounds by RC membranes at MWCO (a) 10kDa, (b) 30kDa, (c) 100kDa

3.3 Analyses of Membrane Fouling

Figure 4 presents the time course of permeate flux for orange juice ultrafiltration using RC membranes with three different MWCO. The initial permeate flux of *ca.* 42 to 29 L m^{-2} h^{-1} decreased gradually with filtration time. The permeate flux declined gradually with time until it reached a steady-state value. All membranes displayed steady-state permeate flux at *ca*. 22 L m^{-2} h^{-1}. The decrease of permeate flux can be explained by the effect of fouling [13].

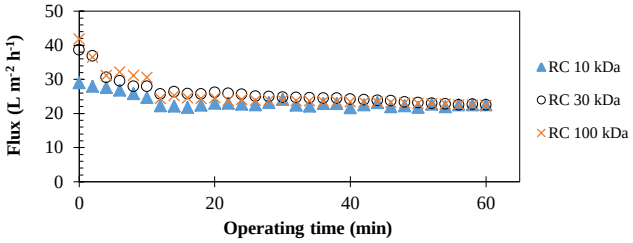

Figure 4. Time course of permeate flux

4. CONCLUSION

The isolation of phytosterols from orange juice has been studied by using RC membranes with 10 kDa, 30 kDa and 100 kDa MWCO. All membranes exhibited steady-state permeate flux values of 22 L m^{-2} h^{-1}. 10 kDa RC membrane gave the lowest rejection of phytosterols. Fouling lead to reduction of the total amount of phytosterol present. The differential rejection of sterol and protein species using a 10 kDa RC membrane indicates that this technology could be suitable for the fractionation and concentration of protein/ sterol mixtures, especially when combined with additional membrane processing steps in series.

ACKNOWLEDGEMENT

The financial support for Nurul Hainiza Abd Razak by the Malaysian Rubber Board (MRB) is gratefully acknowledged. The authors thank Dr. Haofei Guo of *Alfa Laval*, Denmark for kindly supplying the membranes used in this study.

REFERENCES

[1] Marangoni, F., Poli, A., (2010). Phytosterols and cardiovascular health, Pharmacological Research, 61, 3, 193-199.

[2] Shahzad, N., Khan, W., Md, S., Ali, A., Saluja, S.S., Sharma, S., Al-Allaf, F.A., Abduljaleel, Z., Ibrahim, I.A.A., Abdel-Wahab, A.F., Afify, M.A., Al-Ghamdi, S.S., (2017). Phytosterols as a natural anticancer agent: Current status and future perspective, Biomedicine & Pharmacotherapy, 88, Supplement C, 786-794.

[3] Hasma, H., Subramaniam, A., (1986). Composition of lipids in latex of Hevea Brasiliensis clone RRIM 501, Journal of Natural Rubber Research, 1, 30-40.

[4] Jiménez-Escrig, A., Santos-Hidalgo, A.B., Saura-Calixto, F., (2006). Common sources and estimated intake of plant sterols in the Spanish diet, Journal of Agricultural and Food Chemistry, 54, 9, 3462-3471.

[5] Almanasrah, M., Brazinha, C., Kallioinen, M.,Duarte, L.C., Roseiro, L.B., Bogel-Lukasik, R., Carvalheiro, F., Mänttäri, M.,Crespo, J.G., (2015). Nanofiltration and reverse osmosis as a platform for production of natural botanic extracts:The case study of carob by-products, Separation and Purification Technology, 149, 389-397.

[6] Argyle, I.S., Pihlajamäki,A., Bird, M.R., (2015). Black tea liquor ultrafiltration: Effect of ethanol pre-treatment upon fouling and cleaning characteristics, Food and Bioproducts Processing, 93, Supplement C, 289-297.

[7] Mbaebie, B.O., Edeoga H.O., Afolayan, A.J., (2012). Phytochemical analysis and antioxidants activities of aqueous stem bark extract of Schotia latifolia Jacq, Asian Pacific Journal of Tropical Biomedicine, 2, 2, 118-124.
[8] Mulder, M., (1996). Basic Principles of Membrane Technology, Second ed., Kluwer Academic Publishers, The Netherlands.
[9] Abd-Razak, N.H., Chew, Y.M.J., Bird, M.R., (2018). Membrane fouling during the fractionation of phytosterols isolated from orange juice, Food and Bioproducts Processing. *in press*, https://doi.org/10.1016/j.fbp.2018.09.005.
[10] Sass-Kiss, A., Sass, M., (2000). Immunoanalytical method for quality control of orange juice products, J Agric Food Chem, 48, 9, 4027-4031.
[11] Evans, P.J., Bird, M.R., Pihlajamäki, A., Nyström, M., (2008). The influence of hydrophobicity, roughness and charge upon ultrafiltration membranes for black tea liquor clarification, Journal of Membrane Science, 313, 1, 250-262.
[12] Stinco, C.M., Fernández-Vázquez, R., Escudero-Gilete, M.L., Heredia, F.J., Meléndez-Martínez, A.J., Vicario, I.M., (2012). Effect of orange juice's processing on the color, particle size, and bioaccessibility of carotenoids, Journal of Agricultural and Food Chemistry, 60, 6, 1447-1455.
[13] Conidi, C., Cassano, A., Caiazzo, F., Drioli, E., (2017). Separation and purification of phenolic compounds from pomegranate juice by ultrafiltration and nanofiltration membranes, Journal of Food Engineering, 195, 1-13.